

# Koopman–von Neumann Molecular Dynamics for Green–Kubo Transport Coefficients

Masari Watanabe<sup>1,2,\*</sup>, Hirofumi Nishi<sup>1,2</sup>, Taichi Kosugi<sup>1,2</sup>,  
Shigekazu Hidaka<sup>3</sup>, Ryo Sakurai<sup>4</sup>, and Yu-ichiro Matsushita<sup>1,2,5</sup>

<sup>1</sup>Quemix Inc., Taiyo Life Nihonbashi Building, 2-11-2, Nihonbashi Chuo-ku, Tokyo 103-0027, Japan

<sup>2</sup>Department of Physics, The University of Tokyo, Hongo, Bunkyo-ku, Tokyo 113-0033, Japan

<sup>3</sup>Advanced Research and Innovation Center, DENSO CORPORATION,  
500-1 Minamiyama, Komenoki-cho, Nisshin, Aichi 470-0111, Japan

<sup>4</sup>Advanced Research and Innovation Center, DENSO CORPORATION,  
1-1-4, Haneda Airport, Ota-ku, Tokyo 144-0041, Japan

<sup>5</sup>Quantum Materials and Applications Research Center,  
National Institutes for Quantum Science and Technology, Tokyo 152-8550, Japan

(Dated: May 29, 2026)

We formulate the Green–Kubo transport coefficients of classical molecular dynamics as a readout problem for quantum algorithms using the Koopman–von Neumann (KvN) representation. Both NVE and Nosé–Hoover-type NVT dynamics are derived as unitary evolutions on Hilbert spaces associated with the corresponding classical phase spaces. Numerical benchmarks on finite grids show that the discretization error in the correlation function decreases as a power law in the number of grid points  $N_z$ . Equivalently, with  $N_z = 2^{n_z}$ , the error decreases exponentially in the register size  $n_z$ , so a target accuracy  $\epsilon$  requires  $n_z = \mathcal{O}(\log(1/\epsilon))$  qubits. To read out a transport coefficient, we input a flux-excited state to quantum phase estimation (QPE). The probability  $P_0$  of measuring the QPE ancilla register in the all-zero state corresponds to a Bartlett-windowed Green–Kubo integral. With maximum-likelihood amplitude estimation, the statistical estimation of  $P_0$  defined by this QPE oracle improves from the  $N_{\text{queries}}^{-1/2}$  scaling of direct shot sampling to scaling close to  $N_{\text{queries}}^{-1}$ . Our circuit-resource analysis shows that one step of the NVE propagator can be built with  $\mathcal{O}(n^2)$  CX gates, where  $n = n_x + n_p$  is the total number of position and momentum qubits. For the NVT propagator, the centered-difference Pauli-decomposition implementation of the Nosé–Hoover friction term scales as  $\mathcal{O}(n_\xi n_p 2^{n_p})$ , where  $n_p$  and  $n_\xi$  are the numbers of momentum and thermostat qubits, respectively. The proposed framework is a concrete step toward translating the principles of quantum algorithms into the transport-coefficient calculations required in practical molecular simulation.

## I. INTRODUCTION

Molecular dynamics (MD) is a powerful simulation tool for evaluating equilibrium structures, dynamical correlations, and transport coefficients by numerically integrating the equations of motion of atomic nuclei. Diffusion and viscosity coefficients are obtained from Green–Kubo relations as time integrals of equilibrium flux correlation functions [1]. Such calculations are routine in materials design. In lithium-ion batteries, for example, MD is used to evaluate  $\text{Li}^+$  diffusion coefficients in cathode materials, solid electrolytes, and solid-electrolyte interphases, which govern charge–discharge rates and ionic conductivity [2–4]. However, computing transport coefficients, including diffusion coefficients, requires long-time averaging of correlation functions, and convergence of statistical errors requires either long trajectories or many independent samples.

Most work on simulating molecular systems with quantum computers has focused on electronic-structure calculations, the real-time evolution of quantum-chemical Hamiltonians, and the quantum dynamics of chemical reactions [5–8]. Recently, frameworks based on the

Koopman–von Neumann (KvN) representation have been proposed for treating classical Liouville dynamics on quantum computers, along with quantum algorithms for coupled quantum–classical dynamics involving classical nuclei and quantum electrons [9–11]. These studies have mainly targeted properties of the equilibrium distribution, such as thermodynamic quantities and free-energy differences. By contrast, Green–Kubo transport coefficients require not only the equilibrium distribution but also the real-time correlation function of a state excited by a flux operator. In this respect, transport-coefficient evaluation is a readout problem distinct from equilibrium averages and free-energy calculations.

The requirement of physical-time evolution therefore guides the starting point of our formulation. Nosé’s extended Hamiltonian provides a standard way to treat the canonical distribution as a Hamiltonian flow, and it has also been used in Liouvillian-type quantum algorithms for canonical ensembles and free-energy calculations [10–12]. However, the natural evolution parameter of the Nosé Hamiltonian is a scaled auxiliary time rather than physical time. For Green–Kubo integrals, however, the time variable entering the correlation function must be physical time. To avoid this mismatch, we start from the Nosé–Hoover equations, in which the time scaling has been absorbed [1, 13]. Nosé–Hoover dynamics are formulated in physical time, but their phase-space flow is

\* [mwatanabe@quemix.com](mailto:mwatanabe@quemix.com)

compressible. Consequently, a Hermitian KvN generator must be derived from the generalized Liouville equation rather than from the incompressible Hamiltonian Liouville operator.

The KvN representation expresses classical Liouville evolution as linear unitary evolution in Hilbert space [14, 15]. This linearization allows phase-space distributions, flux operators, and time-correlation functions to be treated in the same Hilbert space. In this paper, we use this structure to map Green–Kubo transport coefficients in MD to a readout problem in quantum phase estimation (QPE).

The main results are threefold. First, we derive KvN generators for NVE dynamics and Nosé–Hoover-type NVT dynamics within the same framework and construct the corresponding one-step quantum circuits. Second, assuming that a canonical-state-preparation oracle provides the equilibrium state, we show that, when the flux-excited state is input to QPE, the bin-zero probability  $P_0$  that the probability  $P_0$  of measuring the QPE ancilla register in the all-zero state corresponds to a Bartlett-windowed Green–Kubo integral. Third, we numerically verify that maximum-likelihood amplitude estimation (MLAE) improves the statistical estimation of this  $P_0$  from the  $N_{\text{queries}}^{-1/2}$  scaling of direct shot sampling to scaling close to  $N_{\text{queries}}^{-1}$  [16–18]. Our resource analysis also shows that one step of the NVE propagator can be implemented with  $\mathcal{O}(n^2)$  CX gates, where  $n = n_x + n_p$  is the total number of position and momentum qubits. For the NVT propagator, the centered-difference Pauli-decomposition implementation of the Nosé–Hoover friction term scales as  $\mathcal{O}(n_\xi n_p 2^{n_p})$ , where  $n_p$  and  $n_\xi$  are the numbers of momentum and thermostat qubits, respectively.

Figure 1 conceptually illustrates the readout workflow used in this paper. The real-time dynamics of classical MD are mapped to unitary evolution in KvN-MD, and the time evolution of the flux-excited state is input to QPE. As shown below, the bin-zero probability in QPE corresponds to a Bartlett-windowed Green–Kubo integral.

## II. FORMULATION OF KVN-MD WITH A NOSÉ–HOOVER THERMOSTAT

In this section, we map classical molecular dynamics to the Koopman–von Neumann (KvN) representation and describe both NVE and Nosé–Hoover-type NVT dynamics as unitary time evolutions on a Hilbert space. The KvN representation originates from the Hilbert-space formulation of classical mechanics by Koopman and von Neumann, and it has recently been revisited as a framework for treating classical nonlinear dynamics on quantum computers [9, 14, 15, 19]. We denote the physical phase-space variables by  $\{q_i, p_i\}_{i=1}^{N_f}$ , where  $N_f$  is the number of physical degrees of freedom. Here,  $q_i$  and  $p_i$

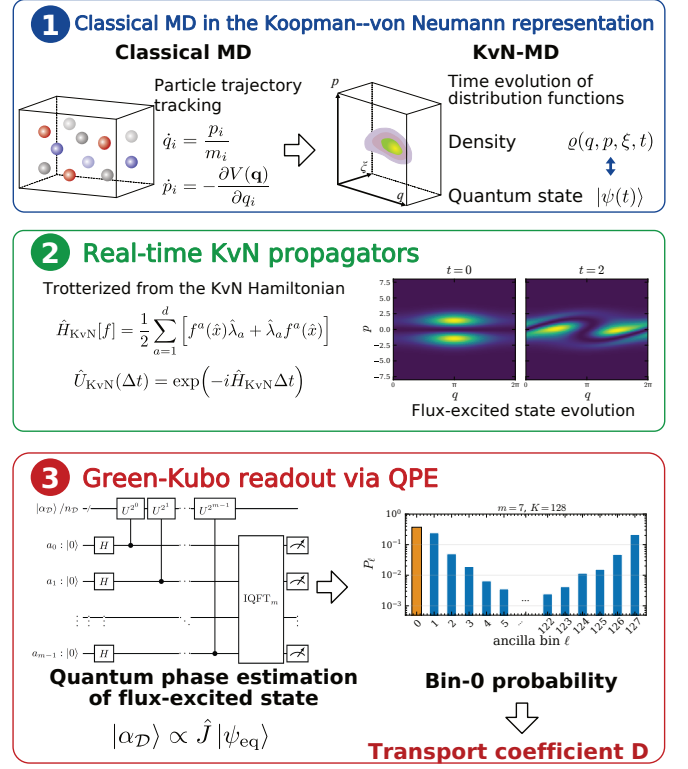


FIG. 1. **Conceptual diagram of Green–Kubo transport-coefficient readout using KvN-MD and QPE.** The phase-space density of classical MD is represented as a KvN wave function, and NVE or Nosé–Hoover-type NVT dynamics are treated as a real-time KvN propagator. When the time evolution of the flux-excited state is input to QPE, a Bartlett-windowed Green–Kubo estimator is obtained from the bin-zero probability of the ancilla register.

are the  $i$ -th position and momentum. In the KvN Hilbert space, hats denote operators acting on phase-space amplitudes. The operators  $\hat{q}_i$ ,  $\hat{p}_i$ , and  $\hat{\xi}$  act by multiplication, while their conjugate derivative operators are defined as

$$\hat{\lambda}_{q_i} = -i \frac{\partial}{\partial q_i}, \quad \hat{\lambda}_{p_i} = -i \frac{\partial}{\partial p_i}. \quad (1)$$

They satisfy

$$[\hat{q}_i, \hat{\lambda}_{q_j}] = i \delta_{ij}, \quad [\hat{p}_i, \hat{\lambda}_{p_j}] = i \delta_{ij}, \quad (2)$$

with all other canonical commutators between different phase-space coordinates vanishing. The variable  $\xi$  is the Nosé–Hoover thermostat friction variable.

Our aim is to construct a Hermitian KvN generator for compressible phase-space flows generated by thermostat dynamics. In particular, the Nosé–Hoover friction term  $-\xi p_i$  gives rise to

$$\hat{H}_3 = -\hat{\xi} \sum_{i=1}^{N_f} \hat{D}_{p_i}, \quad \hat{D}_{p_i} = \frac{1}{2} \left( \hat{p}_i \hat{\lambda}_{p_i} + \hat{\lambda}_{p_i} \hat{p}_i \right). \quad (3)$$

This dilation term is the main operator that distinguishes NVE from NVT in the circuit-resource analysis below.

### A. Generalized Liouville Equation and the KvN Representation

Let  $x = (x^1, \dots, x^d)$  be a coordinate vector that specifies a point in the classical phase space. Here,  $d$  is the dimension of the phase space used to describe the classical flow. For example, for physical NVE dynamics with  $N_f$  degrees of freedom, one may take  $x = (q_1, \dots, q_{N_f}, p_1, \dots, p_{N_f})$  and hence  $d = 2N_f$ . For Nosé-Hoover-type thermostat dynamics,  $x$  may additionally include thermostat variables such as  $\xi$ , and  $d$  is enlarged accordingly. We write the deterministic equations of motion as

$$\dot{x}^a = f^a(x), \quad a = 1, \dots, d. \quad (4)$$

Here,  $f(x) = (f^1(x), \dots, f^d(x))$  is the phase-space velocity vector field, and  $f^a(x)$  denotes its component along the coordinate  $x^a$ . Throughout this section, we use the shorthand  $\partial_a = \partial/\partial x^a$ . Let  $\varrho(x, t)$  denote the probability density at the phase-space point  $x$  and time  $t$ , defined with respect to the flat phase-space volume element  $d^d x = dx^1 \cdots dx^d$ . Conservation of probability is expressed by the continuity equation

$$\frac{\partial \varrho(x, t)}{\partial t} + \sum_{a=1}^d \frac{\partial}{\partial x^a} [f^a(x) \varrho(x, t)] = 0. \quad (5)$$

This form of the Liouville equation applies also to compressible, non-Hamiltonian flows. Expanding the divergence term gives

$$\begin{aligned} \frac{\partial \varrho(x, t)}{\partial t} &= - \sum_{a=1}^d f^a(x) \partial_a \varrho(x, t) - \kappa(x) \varrho(x, t), \\ \kappa(x) &= \sum_{a=1}^d \partial_a f^a(x). \end{aligned} \quad (6)$$

Here,  $\kappa(x)$  is the phase-space compressibility, namely the divergence of the flow field  $f(x)$ . For canonical Hamiltonian dynamics,  $\kappa(x) = 0$ , whereas thermostat dynamics can give  $\kappa(x) \neq 0$ . The compressibility term is therefore essential. Omitting it would break probability conservation at the density level and, in the KvN representation, would correspond to using a non-Hermitian generator [1].

More generally, one may introduce a weighted phase-space measure  $\mu(x) d^d x$ , with  $\mu(x) > 0$ , and regard  $\rho(x, t)$  as a density with respect to that measure. The density with respect to the flat measure is then  $\varrho = \mu \rho$ , and the generalized Liouville equation can be written as

$$\frac{\partial}{\partial t} [\mu(x) \rho(x, t)] + \sum_{a=1}^d \frac{\partial}{\partial x^a} [\mu(x) \rho(x, t) f^a(x)] = 0. \quad (7)$$

Equivalently, in terms of  $\rho$ , this equation becomes

$$\begin{aligned} \frac{\partial \rho(x, t)}{\partial t} &= - \sum_{a=1}^d f^a(x) \partial_a \rho(x, t) - \rho(x, t) \kappa_\mu(x), \\ \kappa_\mu(x) &= \frac{1}{\mu(x)} \sum_{a=1}^d \partial_a [\mu(x) f^a(x)]. \end{aligned} \quad (8)$$

In particular, a weight  $\mu$  satisfying  $\kappa_\mu = 0$  defines an invariant measure of the flow, and the density  $\rho$  with respect to that measure obeys a pure advection equation. In the quantum registers used in this work, however, amplitudes on the discrete grid are normalized so as to represent the square root of the physical density  $\varrho$  with respect to the flat measure. We therefore use, in what follows, the Hermitian generator corresponding to Eq. (5).

In the KvN representation, the probability density is written as the squared modulus of a wave function,

$$\varrho(x, t) = |\psi(x, t)|^2. \quad (9)$$

Defining the operator conjugate to  $x^a$  by

$$\hat{\lambda}_a = -i \frac{\partial}{\partial x^a}, \quad [\hat{x}^a, \hat{\lambda}_b] = i \delta_{ab}. \quad (10)$$

the Hermitian KvN generator that reproduces Eq. (5) is [9, 19]

$$\begin{aligned} \hat{H}_{\text{KvN}}[f] &= \frac{1}{2} \sum_{a=1}^d [f^a(\hat{x}) \hat{\lambda}_a + \hat{\lambda}_a f^a(\hat{x})] \\ &= \sum_{a=1}^d f^a(\hat{x}) \hat{\lambda}_a - \frac{i}{2} \sum_{a=1}^d \partial_a f^a(\hat{x}). \end{aligned} \quad (11)$$

Indeed, the Schrödinger-type equation generated by this operator,

$$i \frac{\partial}{\partial t} |\psi(t)\rangle = \hat{H}_{\text{KvN}}[f] |\psi(t)\rangle. \quad (12)$$

In the coordinate representation, the KvN wavefunction is defined as  $\psi(x, t) = \langle x | \psi(t) \rangle$ . Equation (12) then implies

$$\frac{\partial \psi(x, t)}{\partial t} = - \sum_{a=1}^d f^a(x) \partial_a \psi(x, t) - \frac{1}{2} \left[ \sum_{a=1}^d \partial_a f^a(x) \right] \psi(x, t). \quad (13)$$

Equivalently, using the phase-space compressibility  $\kappa(x) = \sum_{a=1}^d \partial_a f^a(x)$ , this equation can be written as

$$\frac{\partial \psi(x, t)}{\partial t} = - \sum_{a=1}^d f^a(x) \partial_a \psi(x, t) - \frac{1}{2} \kappa(x) \psi(x, t). \quad (14)$$

Therefore, the probability density  $\varrho(x, t) = |\psi(x, t)|^2$  obeys Eq. (5). When  $\kappa(x) = 0$ , as in canonical Hamiltonian flows, Eq. (11) reduces to the usual incompressible-flow Liouville operator  $\sum_{a=1}^d f^a(\hat{x}) \hat{\lambda}_a$ , where  $\hat{\lambda}_a = -i \partial_a$  in the  $x$  representation.

For the physical phase-space variables, we write  $x = (q, p) = (q_1, \dots, q_{N_f}, p_1, \dots, p_{N_f})$ , where  $q_i$  and  $p_i$  are the  $i$ th coordinate and its conjugate momentum. Thus,  $x$  is the phase-space coordinate vector, while  $q$  and  $p$  denote its coordinate and momentum components, respectively.

A key feature of this construction is that the position operators  $\hat{q}_i$  and momentum operators  $\hat{p}_i$  are not the non-commuting canonical operators of quantum mechanics. Rather, they are mutually commuting classical phase-space coordinates represented as multiplication operators on the KvN Hilbert space. Their conjugate derivative operators are

$$[\hat{q}_i, \hat{p}_j] = 0, \quad [\hat{q}_i, \hat{\lambda}_{q_j}] = i\delta_{ij}, \quad [\hat{p}_i, \hat{\lambda}_{p_j}] = i\delta_{ij}. \quad (15)$$

A classical observable  $A(q, p)$  acts as the multiplication operator  $\hat{A} = A(\hat{q}, \hat{p})$  on the KvN Hilbert space. In the  $(q, p)$  representation, the KvN wavefunction is  $\psi(q, p, t) = \langle q, p | \psi(t) \rangle$ , and the associated probability density is  $\varrho(q, p, t) = |\psi(q, p, t)|^2$ . The corresponding classical average at time  $t$  is therefore written as

$$\langle A \rangle_{\varrho(t)} = \int A(q, p) \varrho(q, p, t) d^{N_f} q d^{N_f} p = \langle \psi(t) | \hat{A} | \psi(t) \rangle. \quad (16)$$

This correspondence between the classical probability density  $\varrho(q, p, t)$  and the Hilbert-space norm of  $|\psi(t)\rangle$  is what later allows Green–Kubo correlation functions to be read as inner products in a quantum circuit.

### B. NVE KvN Generator

We first consider NVE dynamics for the physical phase-space variables  $\mathbf{q} = (q_1, \dots, q_{N_f})$  and  $\mathbf{p} = (p_1, \dots, p_{N_f})$ , where  $N_f$  is the number of classical degrees of freedom. The classical Hamiltonian is

$$H_{\text{cl}}(\mathbf{q}, \mathbf{p}) = \sum_{i=1}^{N_f} \frac{p_i^2}{2m_i} + V(\mathbf{q}). \quad (17)$$

The system evolves on the potential-energy surface  $V(\mathbf{q})$ . The force acting on the  $i$ th degree of freedom is defined by

$$F_i(\mathbf{q}) = -\frac{\partial V(\mathbf{q})}{\partial q_i}. \quad (18)$$

The equations of motion are therefore

$$\dot{q}_i = \frac{p_i}{m_i}, \quad \dot{p}_i = F_i(\mathbf{q}), \quad i = 1, \dots, N_f. \quad (19)$$

This Hamiltonian flow is divergence-free in the phase-space coordinates  $(\mathbf{q}, \mathbf{p})$ . Hence, the KvN generator contains no compressibility term and is given by

$$\hat{H}_{\text{KvN}}^{\text{NVE}} = \sum_{i=1}^{N_f} \frac{\hat{p}_i}{m_i} \hat{\lambda}_{q_i} + \sum_{i=1}^{N_f} F_i(\hat{\mathbf{q}}) \hat{\lambda}_{p_i} \equiv \hat{H}_1 + \hat{H}_2. \quad (20)$$

### C. KvN Generator for the Nosé–Hoover Thermostat

To describe the canonical ensemble, we introduce the Nosé–Hoover thermostat variable  $\xi$  in addition to the physical phase-space variables  $\mathbf{q} = (q_1, \dots, q_{N_f})$  and  $\mathbf{p} = (p_1, \dots, p_{N_f})$  [1, 12, 13]. Here,  $q_i$  and  $p_i$  are the position and momentum of the  $i$ th degree of freedom, respectively. We denote the extended phase-space coordinate by  $\mathbf{z} = (\mathbf{q}, \mathbf{p}, \xi)$ .

The single-stage Nosé–Hoover equations are

$$\begin{aligned} \dot{q}_i &= \frac{p_i}{m_i}, \\ \dot{p}_i &= F_i(\mathbf{q}) - \xi p_i, \\ \dot{\xi} &= \frac{1}{Q} \left( \sum_{i=1}^{N_f} \frac{p_i^2}{m_i} - N_f T_0 \right). \end{aligned} \quad (21)$$

Here,  $Q$  is the thermostat mass,  $T_0$  is the target temperature, and we use units with  $k_B = 1$ . Because of the friction term  $-\xi p_i$ , the momenta are damped for  $\xi > 0$  and amplified for  $\xi < 0$ . Equation (21) defines a deterministic flow on the extended phase space,

$$\dot{\mathbf{z}} = \mathbf{f}_{\text{NH}}(\mathbf{z}), \quad (22)$$

where  $\mathbf{f}_{\text{NH}}(\mathbf{z})$  is the Nosé–Hoover vector field whose components are given by the right-hand sides of Eq. (21).

The phase-space compressibility of the Nosé–Hoover flow is the divergence of  $\mathbf{f}_{\text{NH}}(\mathbf{z})$  in the extended variables  $\mathbf{z} = (\mathbf{q}, \mathbf{p}, \xi)$ :

$$\kappa_{\text{NH}}(\mathbf{z}) = -N_f \xi. \quad (23)$$

For the extended canonical density

$$\begin{aligned} \varrho_{\text{ext}}(\mathbf{q}, \mathbf{p}, \xi) &\propto \exp \left[ -\beta \left( H_{\text{cl}}(\mathbf{q}, \mathbf{p}) + \frac{Q\xi^2}{2} \right) \right], \\ \beta &= T_0^{-1}, \end{aligned} \quad (24)$$

a direct calculation gives

$$\mathbf{f}_{\text{NH}}(\mathbf{z}) \cdot \nabla_{\mathbf{z}} \log \varrho_{\text{ext}}(\mathbf{q}, \mathbf{p}, \xi) = N_f \xi = -\kappa_{\text{NH}}(\mathbf{z}). \quad (25)$$

It follows from Eq. (6) that

$$\nabla_{\mathbf{z}} \cdot [\mathbf{f}_{\text{NH}}(\mathbf{z}) \varrho_{\text{ext}}(\mathbf{q}, \mathbf{p}, \xi)] = 0. \quad (26)$$

Thus, Eq. (24) is an invariant density of the Nosé–Hoover flow. After integrating out  $\xi$ , the marginal distribution on  $(\mathbf{q}, \mathbf{p})$  is the usual canonical distribution proportional to  $\exp[-\beta H_{\text{cl}}(\mathbf{q}, \mathbf{p})]$ .

The existence of an invariant density, however, does not imply that the density can be sampled efficiently from an arbitrary initial state. The ergodicity of a single-stage Nosé–Hoover trajectory can fail in low-dimensional or strongly integrable systems, and Nosé–Hoover chains are often used for practical canonical sampling [1, 20]. In

this work, we use the single-stage Nosé–Hoover equations as the reference case in order to clarify the structure of the KvN generator and its quantum-circuit implementation for thermostatted classical flows. In an extension to a multistage chain, dilation-type terms of the same kind arise from the couplings between thermostat variables. Thus, the essential circuit-level difficulty is already represented by the  $\hat{H}_3$  term derived below.

Because Eq. (21) defines a compressible flow on the extended phase space  $\mathbf{z} = (\mathbf{q}, \mathbf{p}, \xi)$ , the unsymmetrized Liouville operator used for divergence-free NVE dynamics is no longer Hermitian. We therefore apply the symmetrized KvN construction in Eq. (11) to each component of the Nosé–Hoover vector field  $\mathbf{f}_{\text{NH}}(\mathbf{z})$ . The contributions from the  $\mathbf{q}$ -component advection, the conservative force-induced  $\mathbf{p}$ -component advection, and the  $\xi$ -component advection are, respectively,

$$\hat{H}_1 = \sum_{i=1}^{N_f} \frac{\hat{p}_i}{m_i} \hat{\lambda}_{q_i}. \quad (27)$$

$$\hat{H}_2 = \sum_{i=1}^{N_f} F_i(\hat{\mathbf{q}}) \hat{\lambda}_{p_i}. \quad (28)$$

$$\hat{H}_4 = \frac{1}{Q} \left( \sum_{i=1}^{N_f} \frac{\hat{p}_i^2}{m_i} - N_f T_0 \right) \hat{\lambda}_\xi. \quad (29)$$

Because each coefficient in Eqs. (27)–(29) is independent of its corresponding differentiation variable, the symmetrization generates no additional terms for these three contributions.

The nontrivial contribution comes from the friction part  $-\xi p_i$  of the  $p_i$  equation of motion. Applying Eq. (11) to this component gives

$$\frac{1}{2} \left[ (-\hat{\xi} \hat{p}_i) \hat{\lambda}_{p_i} + \hat{\lambda}_{p_i} (-\hat{\xi} \hat{p}_i) \right] = -\hat{\xi} \frac{1}{2} \left( \hat{p}_i \hat{\lambda}_{p_i} + \hat{\lambda}_{p_i} \hat{p}_i \right). \quad (30)$$

Thus, defining the Hermitian dilation generator in the  $p_i$  direction as

$$\hat{D}_{p_i} \equiv \frac{1}{2} \left( \hat{p}_i \hat{\lambda}_{p_i} + \hat{\lambda}_{p_i} \hat{p}_i \right), \quad (31)$$

the thermostat-specific contribution is

$$\hat{H}_3 = -\hat{\xi} \sum_{i=1}^{N_f} \hat{D}_{p_i}. \quad (32)$$

Combining these terms, the NVT KvN generator decomposes as

$$\hat{H}_{\text{KvN}}^{\text{NVT}} = \hat{H}_1 + \hat{H}_2 + \hat{H}_3 + \hat{H}_4. \quad (33)$$

#### D. Meaning of the Dilation Operator and NVT Time Evolution

The operator  $\hat{D}_p$  is the generator of dilations in momentum space. In the continuous representation,

$$\hat{D}_p = \frac{1}{2} (p(-i\partial_p) + (-i\partial_p)p) = -i \left( p\partial_p + \frac{1}{2} \right). \quad (34)$$

It follows that

$$e^{-ia\hat{D}_p}\psi(p) = e^{-a/2}\psi(e^{-a}p), \quad (35)$$

so the wave-function amplitude is rescaled along the momentum axis while the norm is preserved. For the partial evolution generated by  $\hat{H}_3 = -\xi\hat{D}_p$ , one has  $a = -\xi\Delta t$ . Hence a peak initially located at momentum  $p$  is shifted to

$$p(t + \Delta t) = e^{-\xi\Delta t}p(t),$$

in agreement with the classical solution of  $\dot{p} = -\xi p$ . This corresponds to cooling for  $\xi > 0$  and heating for  $\xi < 0$ .

Starting from the generalized Liouville equation, we have thus obtained Hermitian KvN generators for both NVE and Nosé–Hoover-type NVT dynamics. In the quantum circuits below, the corresponding one-step propagators serve as the basic building blocks.

### III. QUANTUM CIRCUIT IMPLEMENTATION

In this section, we translate the KvN generators derived in the previous section into quantum circuit blocks for their one-step time evolutions. To keep the notation compact for many-particle systems, we collect all position and momentum degrees of freedom into the bundled registers

$$|\mathbf{q}\rangle = |q_1, \dots, q_{N_f}\rangle, \quad |\mathbf{p}\rangle = |p_1, \dots, p_{N_f}\rangle. \quad (36)$$

We denote the corresponding total numbers of qubits by  $n_q$  and  $n_p$ . For Nosé–Hoover-type NVT dynamics, we also introduce the thermostat register  $|\xi\rangle$ , with  $n_\xi$  qubits. The operators  $\mathcal{F}_q$  and  $\mathcal{F}_p$  denote tensor products of QFTs acting on all  $q_i$  and  $p_i$  registers, respectively. The operators  $\hat{k}_{q_i}$  and  $\hat{k}_{p_i}$  are the corresponding discrete conjugate wavenumber operators in the Fourier-transformed bases. When the thermostat register is Fourier transformed, we use the analogous notation  $\mathcal{F}_\xi$  and  $\hat{k}_\xi$ .

#### A. One-Step Propagator

For each partial generator  $\hat{H}_j$ , we define the corresponding short-time propagator as

$$U_j(\delta t) = \exp[-i\delta t\hat{H}_j]. \quad (37)$$

For the time discretization, we use the standard second-order symmetric Suzuki–Trotter product formula of quantum simulation [21–25].

For NVE dynamics, the KvN generator is decomposed as  $\hat{H}_{\text{KvN}}^{\text{NVE}} = \hat{H}_1 + \hat{H}_2$ , where

$$\begin{aligned}\hat{H}_1 &= \sum_{i=1}^{N_f} \frac{\hat{p}_i}{m_i} \hat{\lambda}_{q_i}, \\ \hat{H}_2 &= \sum_{i=1}^{N_f} F_i(\hat{\mathbf{q}}) \hat{\lambda}_{p_i}.\end{aligned}\quad (38)$$

The terms within each sum mutually commute. Therefore, the many-degree-of-freedom propagator can be written in the same drift–kick–drift form as in the single-degree-of-freedom case, with all position degrees of freedom updated collectively by a half step, all momentum degrees of freedom updated collectively by a full step, and the position degrees of freedom updated again by a half step:

$$S_2^{\text{NVE}}(\Delta t) = U_1(\Delta t/2)U_2(\Delta t)U_1(\Delta t/2). \quad (39)$$

By the Baker–Campbell–Hausdorff expansion, this palindromic product formula satisfies

$$S_2^{\text{NVE}}(\Delta t) = \exp \left[ -i \left( \hat{H}_1 + \hat{H}_2 \right) \Delta t + \mathcal{O}(\Delta t^3) \right]. \quad (40)$$

Equivalently, the local error of one step is  $\mathcal{O}(\Delta t^3)$ , and the global error up to a fixed physical time is  $\mathcal{O}(\Delta t^2)$ . This time-reversal symmetry is useful for the long-time correlation functions considered in this work.

For Nosé–Hoover-type NVT dynamics, the KvN generator is decomposed as  $\hat{H}_{\text{KvN}}^{\text{NVT}} = \hat{H}_1 + \hat{H}_2 + \hat{H}_3 + \hat{H}_4$ , where  $\hat{H}_3$  contains the momentum-dilation generator and  $\hat{H}_4$  generates the thermostat-variable advection:

$$\begin{aligned}\hat{H}_3 &= -\hat{\xi} \sum_{i=1}^{N_f} \hat{D}_{p_i}, \\ \hat{H}_4 &= \frac{1}{Q} \left( \sum_{i=1}^{N_f} \frac{\hat{p}_i^2}{m_i} - N_f T_0 \right) \hat{\lambda}_{\xi}.\end{aligned}\quad (41)$$

Using the same second-order symmetric Suzuki–Trotter construction, we take

$$\begin{aligned}S_2^{\text{NVT}}(\Delta t) &= U_1(\Delta t/2)U_2(\Delta t/2)U_3(\Delta t/2)U_4(\Delta t) \\ &\quad \times U_3(\Delta t/2)U_2(\Delta t/2)U_1(\Delta t/2).\end{aligned}\quad (42)$$

This palindromic product formula satisfies

$$S_2^{\text{NVT}}(\Delta t) = \exp \left[ -i \left( \hat{H}_1 + \hat{H}_2 + \hat{H}_3 + \hat{H}_4 \right) \Delta t + \mathcal{O}(\Delta t^3) \right]. \quad (43)$$

Thus, the local error of one NVT step is also  $\mathcal{O}(\Delta t^3)$ , and the global error up to a fixed physical time is  $\mathcal{O}(\Delta t^2)$ . The term  $\hat{H}_3$  is the central additional component of the

real-time NVT propagator relative to the NVE case, because it contains the momentum-dilation generator induced by the Nosé–Hoover friction. Its quantum-circuit implementation is discussed in the next section.

Figure 2 shows these one-step propagators and the QPE readout circuit.

Figure 2(a) uses diagonal unitaries that act collectively on the bundled coordinate and momentum registers. For the drift generator  $\hat{H}_1$ , the QFT is applied to the coordinate registers  $\mathbf{q} = (q_1, \dots, q_{N_f})$ , so that  $\hat{\lambda}_{q_i}$  is represented by the diagonal Fourier-conjugate operator  $\hat{k}_{q_i}$ . The corresponding diagonal phase is

$$\Phi_q(\delta t) = \exp \left[ -i\delta t \sum_{i=1}^{N_f} \frac{\hat{p}_i}{m_i} \hat{k}_{q_i} \right]. \quad (44)$$

Note that  $\hat{k}_{q_i}$  is the Fourier-conjugate operator associated with the  $q_i$  register, and should not be confused with the physical momentum coordinate  $\hat{p}_i$ .

For the force generator  $\hat{H}_2$ , the QFT is applied to the momentum registers  $\mathbf{p} = (p_1, \dots, p_{N_f})$ , so that  $\hat{\lambda}_{p_i}$  is represented by the diagonal Fourier-conjugate operator  $\hat{k}_{p_i}$ . The corresponding diagonal phase is

$$\Phi_p(\delta t) = \exp \left[ -i\delta t \sum_{i=1}^{N_f} F_i(\hat{\mathbf{q}}) \hat{k}_{p_i} \right]. \quad (45)$$

The force component  $F_i(\hat{\mathbf{q}})$  may depend on all coordinate registers and is therefore implemented as a diagonal function of the bundled coordinate register  $\hat{\mathbf{q}}$ .

For the thermostat-advection generator  $\hat{H}_4$  in the NVT circuit, the QFT is applied to the thermostat register  $\xi$ , so that  $\hat{\lambda}_{\xi}$  is represented by the diagonal Fourier-conjugate operator  $\hat{k}_{\xi}$ . The corresponding diagonal phase is

$$\Phi_{\xi}(\delta t) = \exp \left[ -i\delta t \frac{\sum_{i=1}^{N_f} \hat{p}_i^2/m_i - N_f T_0}{Q} \hat{k}_{\xi} \right]. \quad (46)$$

Thus,  $U_1$ ,  $U_2$ , and  $U_4$  have the QFT–diagonal-phase–inverse-QFT structure used in split-operator quantum simulation [5, 26]. By contrast,  $U_3$  contains the momentum-dilation generator  $\hat{D}_{p_i}$  and is not diagonalized by a simple QFT on a single register. In this work, we implement  $U_3$  using the centered-difference Pauli-decomposition method described in Appendix C.

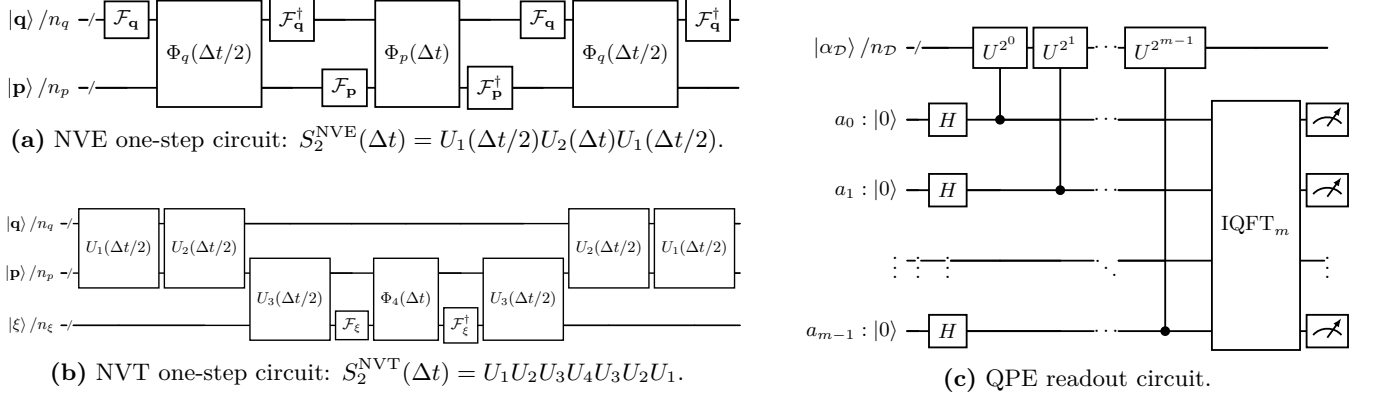


FIG. 2. **Quantum circuits for KvN propagators and QPE readout.** (a) Multi-particle NVE one-step propagator in drift–kick–drift form. The bundled registers  $|\mathbf{q}\rangle$  and  $|\mathbf{p}\rangle$  contain all classical degrees of freedom, and the slash denotes a multi-qubit register. The QFTs  $\mathcal{F}_q$  and  $\mathcal{F}_p$  are tensor products over the corresponding coordinate registers. The diagonal phases are  $\Phi_q(\delta t) = \exp[-i\delta t \sum_i \hat{p}_i \hat{k}_{q_i} / m_i]$  and  $\Phi_p(\delta t) = \exp[-i\delta t \sum_i F_i(\hat{\mathbf{q}}) \hat{k}_{p_i}]$ . (b) Nosé–Hoover NVT one-step propagator. The additional dilation block is  $U_3(\delta t) = \exp[-i\delta t \hat{H}_3]$ , with  $\hat{H}_3 = -\hat{\xi} \sum_i \hat{D}_{p_i}$  and  $\hat{D}_{p_i} = (\hat{p}_i \hat{\lambda}_{p_i} + \hat{\lambda}_{p_i} \hat{p}_i) / 2$ . The thermostat block is implemented as  $\mathcal{F}_\xi^\dagger \Phi_4(\delta t) \mathcal{F}_\xi$ , where  $\Phi_4(\delta t) = \exp[-i\delta t [(\sum_i \hat{p}_i^2 / m_i) - N_f T_0] \hat{k}_\xi / Q]$ . (c) QPE readout circuit. The controlled powers of  $U = S_2^{\mathcal{D}}(\Delta t)$  act on the flux-excited state  $|\alpha_{\mathcal{D}}\rangle \propto \hat{J} |\psi_{\text{eq}, \mathcal{D}}\rangle$ . Here  $n_{\mathcal{D}} = n_q + n_p$  for  $\mathcal{D} = \text{NVE}$  and  $n_{\mathcal{D}} = n_q + n_p + n_\xi$  for  $\mathcal{D} = \text{NVT}$ . The bin-zero probability gives the Bartlett-windowed Green–Kubo integral derived in Sec. V.

## B. State Preparation and the Flux-Excited State

The QPE circuit is initialized with a flux-excited KvN state. For  $\mathcal{D} \in \{\text{NVE}, \text{NVT}\}$ , we define

$$\begin{aligned} \mathbf{z}_{\mathcal{D}} &= \begin{cases} (\mathbf{q}, \mathbf{p}), & \mathcal{D} = \text{NVE}, \\ (\mathbf{q}, \mathbf{p}, \xi), & \mathcal{D} = \text{NVT}, \end{cases} \\ |\mathbf{z}_{\mathcal{D}}\rangle &= \begin{cases} |\mathbf{q}, \mathbf{p}\rangle, & \mathcal{D} = \text{NVE}, \\ |\mathbf{q}, \mathbf{p}, \xi\rangle, & \mathcal{D} = \text{NVT}, \end{cases} \\ d\Gamma_{\mathcal{D}} &= \begin{cases} \prod_{i=1}^{N_f} dq_i dp_i, & \mathcal{D} = \text{NVE}, \\ \left( \prod_{i=1}^{N_f} dq_i dp_i \right) d\xi, & \mathcal{D} = \text{NVT}. \end{cases} \end{aligned} \quad (47)$$

Let  $\varrho_{\text{eq}, \mathcal{D}}(\mathbf{z}_{\mathcal{D}})$  be the normalized equilibrium density,

$$\int \varrho_{\text{eq}, \mathcal{D}}(\mathbf{z}_{\mathcal{D}}) d\Gamma_{\mathcal{D}} = 1. \quad (48)$$

The equilibrium KvN state is defined by

$$\begin{aligned} \psi_{\text{eq}, \mathcal{D}}(\mathbf{z}_{\mathcal{D}}) &= \sqrt{\varrho_{\text{eq}, \mathcal{D}}(\mathbf{z}_{\mathcal{D}})}, \\ |\psi_{\text{eq}, \mathcal{D}}\rangle &= \int \psi_{\text{eq}, \mathcal{D}}(\mathbf{z}_{\mathcal{D}}) |\mathbf{z}_{\mathcal{D}}\rangle d\Gamma_{\mathcal{D}}. \end{aligned} \quad (49)$$

On a discrete quantum register, the integral in Eq. (49) is replaced by the corresponding normalized sum over grid points.

We assume a state-preparation oracle for the normalized flux-excited state

$$|\alpha_{\mathcal{D}}\rangle = \frac{\hat{J} |\psi_{\text{eq}, \mathcal{D}}\rangle}{\sqrt{\langle \psi_{\text{eq}, \mathcal{D}} | \hat{J}^2 | \psi_{\text{eq}, \mathcal{D}} \rangle}}. \quad (50)$$

Here,  $\hat{J}$  is the scalar flux operator used for the target transport coefficient. For the velocity flux of the  $\ell$ th scalar degree of freedom,

$$\hat{J}_\ell = \frac{\hat{p}_\ell}{m_\ell}, \quad \ell = 1, \dots, N_f. \quad (51)$$

A diagonal flux operator  $J(\hat{\mathbf{q}}, \hat{\mathbf{p}})$  can be included by amplitude preparation based on the diagonal function or by an LCU-type state-preparation procedure.

The controlled unitary used in QPE is

$$U = S_2^{\mathcal{D}}(\Delta t), \quad \mathcal{D} \in \{\text{NVE}, \text{NVT}\}. \quad (52)$$

## IV. DYNAMICAL CORRELATIONS

In this section, we define the equilibrium KvN wave function, the flux-excited state, and the velocity autocorrelation function (VACF) needed for Green–Kubo transport coefficients. The KvN inner-product representation is not restricted to NVE dynamics. The same construction applies to Hamiltonian NVE dynamics and to extended-phase-space NVT dynamics with a Nosé–Hoover thermostat, provided that the corresponding invariant distribution and Hermitian KvN generator are specified. In the latter part of this section, we use a two-particle coupled cosine system to verify that the finite-grid VACF converges to a classical MD reference.

### A. Invariant Density and Equilibrium KvN Wave Function

The KvN wavefunction corresponding to Eq. (24) is chosen as the positive square root of the extended canonical density. In the continuum notation, it factorizes as

$$\begin{aligned}\psi_{\text{ext}}(\mathbf{q}, \mathbf{p}, \xi) &= \psi_{\text{can}}(\mathbf{q}, \mathbf{p}) \chi_{\text{th}}(\xi), \\ \psi_{\text{can}}(\mathbf{q}, \mathbf{p}) &= \frac{1}{\sqrt{Z_{\text{can}}}} \exp\left[-\frac{\beta}{2} H_{\text{cl}}(\mathbf{q}, \mathbf{p})\right], \\ \chi_{\text{th}}(\xi) &= \left(\frac{\beta Q}{2\pi}\right)^{1/4} \exp\left[-\frac{\beta Q \xi^2}{4}\right].\end{aligned}\quad (53)$$

Here,  $\chi_{\text{th}}(\xi)$  is the normalized KvN amplitude for the Nosé–Hoover thermostat variable  $\xi$ , and

$$Z_{\text{can}} = \int \exp[-\beta H_{\text{cl}}(\mathbf{q}, \mathbf{p})] \prod_{i=1}^{N_f} dq_i dp_i. \quad (54)$$

Thus, the extended equilibrium KvN state can be written as

$$|\psi_{\text{ext}}\rangle = |\psi_{\text{can}}\rangle_{\mathbf{q}, \mathbf{p}} \otimes |\chi_{\text{th}}\rangle_{\xi}. \quad (55)$$

On a discrete grid, we absorb the grid weights into the normalization constant and use

$$|\psi_{\text{can}}\rangle = \frac{1}{\sqrt{Z_{\text{grid}}}} \sum_{\mathbf{q}, \mathbf{p}} \exp\left[-\frac{\beta}{2} H_{\text{cl}}(\mathbf{q}, \mathbf{p})\right] |\mathbf{q}, \mathbf{p}\rangle, \quad (56)$$

where the sum runs over all discrete grid points of the  $(\mathbf{q}, \mathbf{p})$  registers. The normalization constant  $Z_{\text{can}}$  is defined by

$$Z_{\text{grid}} = \sum_{\mathbf{q}, \mathbf{p}} \exp[-\beta H_{\text{cl}}(\mathbf{q}, \mathbf{p})]. \quad (57)$$

### B. KvN Inner-Product Representation of Green–Kubo Correlation Functions

We consider the velocity autocorrelation function for the  $\ell$ th scalar degree of freedom under the dynamics  $\mathcal{D} \in \{\text{NVE}, \text{NVT}\}$ . The phase-space variable is  $\mathbf{z}_{\mathcal{D}} = (\mathbf{q}, \mathbf{p})$  for  $\mathcal{D} = \text{NVE}$  and  $\mathbf{z}_{\mathcal{D}} = (\mathbf{q}, \mathbf{p}, \xi)$  for  $\mathcal{D} = \text{NVT}$ . The equilibrium expectation value of a classical observable  $A(\mathbf{z}_{\mathcal{D}})$  is

$$\langle A \rangle_{\text{eq}, \mathcal{D}} = \int A(\mathbf{z}_{\mathcal{D}}) \rho_{\text{eq}, \mathcal{D}}(\mathbf{z}_{\mathcal{D}}) d\Gamma_{\mathcal{D}}. \quad (58)$$

For the corresponding multiplication operator  $\hat{A}$ , this expectation value is equivalently written as

$$\langle A \rangle_{\text{eq}, \mathcal{D}} = \langle \psi_{\text{eq}, \mathcal{D}} | \hat{A} | \psi_{\text{eq}, \mathcal{D}} \rangle, \quad (59)$$

where  $|\psi_{\text{eq}, \mathcal{D}}\rangle$  is the equilibrium KvN state.

The velocity component and its multiplication operator are defined by

$$v_{\ell}(\mathbf{z}_{\mathcal{D}}) = \frac{p_{\ell}}{m_{\ell}}, \quad \hat{v}_{\ell} = \frac{\hat{p}_{\ell}}{m_{\ell}}, \quad \ell = 1, \dots, N_f. \quad (60)$$

For  $\mathcal{D} = \text{NVT}$ ,  $\hat{v}_{\ell}$  acts on the physical momentum register and as the identity on the thermostat register. The time-dependent velocity  $v_{\ell}(t; \mathbf{z}_{\mathcal{D}})$  denotes the value of this velocity component at time  $t$  along the classical trajectory initialized at  $\mathbf{z}_{\mathcal{D}}$ . Thus,

$$v_{\ell}(t; \mathbf{z}_{\mathcal{D}}) = \frac{p_{\ell}(t; \mathbf{z}_{\mathcal{D}})}{m_{\ell}}, \quad v_{\ell}(0; \mathbf{z}_{\mathcal{D}}) = \frac{p_{\ell}}{m_{\ell}}. \quad (61)$$

The velocity autocorrelation function is

$$\begin{aligned}C_{vv, \ell}^{\mathcal{D}}(t) &= \langle v_{\ell}(t) v_{\ell}(0) \rangle_{\text{eq}, \mathcal{D}} \\ &= \int v_{\ell}(t; \mathbf{z}_{\mathcal{D}}) v_{\ell}(0; \mathbf{z}_{\mathcal{D}}) \rho_{\text{eq}, \mathcal{D}}(\mathbf{z}_{\mathcal{D}}) d\Gamma_{\mathcal{D}}.\end{aligned}\quad (62)$$

At  $t = 0$ ,

$$C_{vv, \ell}^{\mathcal{D}}(0) = \langle v_{\ell}^2 \rangle_{\text{eq}, \mathcal{D}} = \langle \psi_{\text{eq}, \mathcal{D}} | \hat{v}_{\ell}^2 | \psi_{\text{eq}, \mathcal{D}} \rangle. \quad (63)$$

The normalized velocity-weighted KvN state is

$$|\alpha_{\mathcal{D}, \ell}\rangle = \frac{\hat{v}_{\ell} |\psi_{\text{eq}, \mathcal{D}}\rangle}{\sqrt{\langle \psi_{\text{eq}, \mathcal{D}} | \hat{v}_{\ell}^2 | \psi_{\text{eq}, \mathcal{D}} \rangle}} = \frac{\hat{v}_{\ell} |\psi_{\text{eq}, \mathcal{D}}\rangle}{\sqrt{C_{vv, \ell}^{\mathcal{D}}(0)}}. \quad (64)$$

The KvN time-evolution operator is

$$U_{\mathcal{D}}(t) = \exp\left[-i \hat{H}_{\text{KvN}}^{\mathcal{D}} t\right]. \quad (65)$$

With this convention, the normalized VACF becomes the Hilbert-space autocorrelation function

$$c_{vv, \ell}^{\mathcal{D}}(t) \equiv \frac{C_{vv, \ell}^{\mathcal{D}}(t)}{C_{vv, \ell}^{\mathcal{D}}(0)} = \langle \alpha_{\mathcal{D}, \ell} | U_{\mathcal{D}}(t) | \alpha_{\mathcal{D}, \ell} \rangle. \quad (66)$$

Depending on the sign convention used for the KvN generator, the right-hand side of Eq. (66) may instead give  $c_{vv, \ell}^{\mathcal{D}}(-t)$ . This distinction does not affect the Green–Kubo integral when the equilibrium VACF is real and time-reversal symmetric.

Equation (66) can be evaluated by QPE, or by a Hadamard test with a controlled implementation of  $U_{\mathcal{D}}(t)$ . In the Hadamard-test approach, the real part of  $\langle \alpha_{\mathcal{D}, \ell} | U_{\mathcal{D}}(t) | \alpha_{\mathcal{D}, \ell} \rangle$  gives the normalized VACF.

### C. Validation Setup Using a Two-Particle Coupled Cosine System

To validate the dynamical correlations, we use a two-particle, one-dimensional coupled cosine potential,

$$V(q_1, q_2) = V_0 [\cos(q_1 - q_2) + \varepsilon(\cos q_1 + \cos q_2)]. \quad (67)$$

In the numerical examples, we set  $V_0 = 5$ ,  $\varepsilon = 1.2$ ,  $m = 1$ , and  $T_0 = 1$ .

A single-particle NVE system in a cosine potential is a one-degree-of-freedom Hamiltonian system, and its trajectories are integrable. In particular, running trajectories that cross the barrier give ballistic contributions at long times, making the single-particle model unsuitable as a validation system for transport coefficients associated with normal diffusion. With two particles, the interparticle coupling competes with the external periodic potential. This competition induces energy exchange and nonlinear mixing, promotes chaotic behavior, and produces a normal-diffusive component over finite observation times. For this reason, the present system serves as a minimal model in which the short-time oscillation of the VACF, its long-time decay, and the onset of finite-grid errors can be examined within the same setup.

Each position coordinate is represented on a periodic grid, and  $N_p = 64$  grid points are used for each momentum coordinate. The momentum range is chosen sufficiently wide according to the discretization criteria discussed above. For the number  $N_q$  of position-grid points, we compare  $N_q = 16, 32, 64, 128$  for NVE and  $N_q = 16, 32, 48$  for NVT. For the classical MD reference, canonical initial conditions were sampled by Langevin NVT simulations [27], and the subsequent production runs were performed using either NVE dynamics or single-thermostat Nosé–Hoover dynamics.

For the selected dynamics  $\mathcal{D}$ , the quantity compared in this section is

$$\Delta c_{\mathcal{D}}(t) = c_{\mathcal{D}}^{\text{KvN}}(t) - c_{\mathcal{D}}^{\text{MD}}(t). \quad (68)$$

Here  $c_{\mathcal{D}}^{\text{KvN}}(t)$  is computed from the discrete KvN propagator through Eq. (66), whereas  $c_{\mathcal{D}}^{\text{MD}}(t)$  is the VACF obtained from the corresponding average over classical trajectories. Because a finite number of MD trajectories is used,  $\Delta c_{\mathcal{D}}(t)$  contains not only the finite-grid error on the KvN side but also the statistical error of the MD reference.

For the numerical validation in this work, we applied the matrix operations corresponding to the quantum gates by state-vector simulation using NumPy and CuPy. As shown in Appendix E, the resulting propagators and QPE bin distributions agree with Qiskit [28] statevector simulations to within machine precision.

Figures 3(a)–3(c) show the validation for Hamiltonian NVE evolution. Panel (a) shows the short-time VACF, panel (b) shows the time evolution of  $|\Delta c(t)|/c(0)$ , and panel (c) shows the  $N_q$  dependence of the peak deviation. Figures 3(d)–3(f) show the same analysis for Nosé–Hoover NVT evolution, where the grid convergence of  $C_{vv}(t)$  is evaluated through the KvN inner-product representation on the extended phase space including the thermostat variable.

## D. Finite-Grid Errors and Grid Convergence

Figures 3(a) and 3(d) show the short-time VACF obtained with the NVE and NVT propagators, respectively. In both cases, the curves converge as the position grid is refined, and the short-time oscillatory structure agrees with the classical MD reference. This confirms that, under appropriate discretization conditions, the selected Liouville evolution is stably reproduced by the discrete KvN propagator.

At longer times, finite-grid effects become visible. Figures 3(b) and 3(e) show  $|\Delta c(t)|/c(0)$  on a logarithmic scale. Increasing  $N_q$  delays the onset of error growth. This behavior is analogous to filamentation, which is well known in Vlasov-type grid simulations [29–32]. As the phase-space flow develops increasingly fine structures in the KvN wave function, Fourier components beyond the Nyquist wavenumber of the finite grid can no longer be represented accurately. Increasing the number of grid points delays this onset, but it does not eliminate the finite-grid limitation at arbitrarily long times.

Figures 3(c) and 3(f) show the peak deviation over  $0 \leq t \leq T_{\text{sim}}$  as a function of  $N_q$ . Within the present validation range, we observe the empirical scaling

$$\max_{0 \leq t \leq T_{\text{sim}}} \frac{|\Delta c_{\text{NVE}}(t)|}{c_{\text{NVE}}(0)} \propto N_q^{-1.17}, \quad (69)$$

for NVE, and

$$\max_{0 \leq t \leq T_{\text{sim}}} \frac{|\Delta c_{\text{NVT}}(t)|}{c_{\text{NVT}}(0)} \propto N_q^{-1.57} \quad (70)$$

for NVT. When a lower-statistics MD reference is used, the error reaches a floor at large  $N_q$ . This floor is not a finite-grid error of the KvN calculation, but is caused by statistical noise in the classical trajectory average.

More generally, let  $z$  denote the grid axis that dominates the correlation-function error, and let  $N_z$  be the number of grid points along that axis. Suppose that, over the observation range of interest, the correlation-function error follows

$$\epsilon_C(N_z) \simeq A N_z^{-\gamma}. \quad (71)$$

For a quantum register representation,  $N_z = 2^{n_z}$ , and therefore

$$\epsilon_C(n_z) \simeq A 2^{-\gamma n_z}. \quad (72)$$

The number of qubits required to reach a target error  $\epsilon_C^{\text{target}}$  is then estimated as

$$n_z \gtrsim \frac{1}{\gamma} \log_2 \left( \frac{A}{\epsilon_C^{\text{target}}} \right). \quad (73)$$

The exponents  $\gamma = 1.17$  and  $1.57$  in Fig. 3 are empirical values for the present validation system, not universal convergence exponents. The essential point is that algebraic convergence with respect to the number of grid

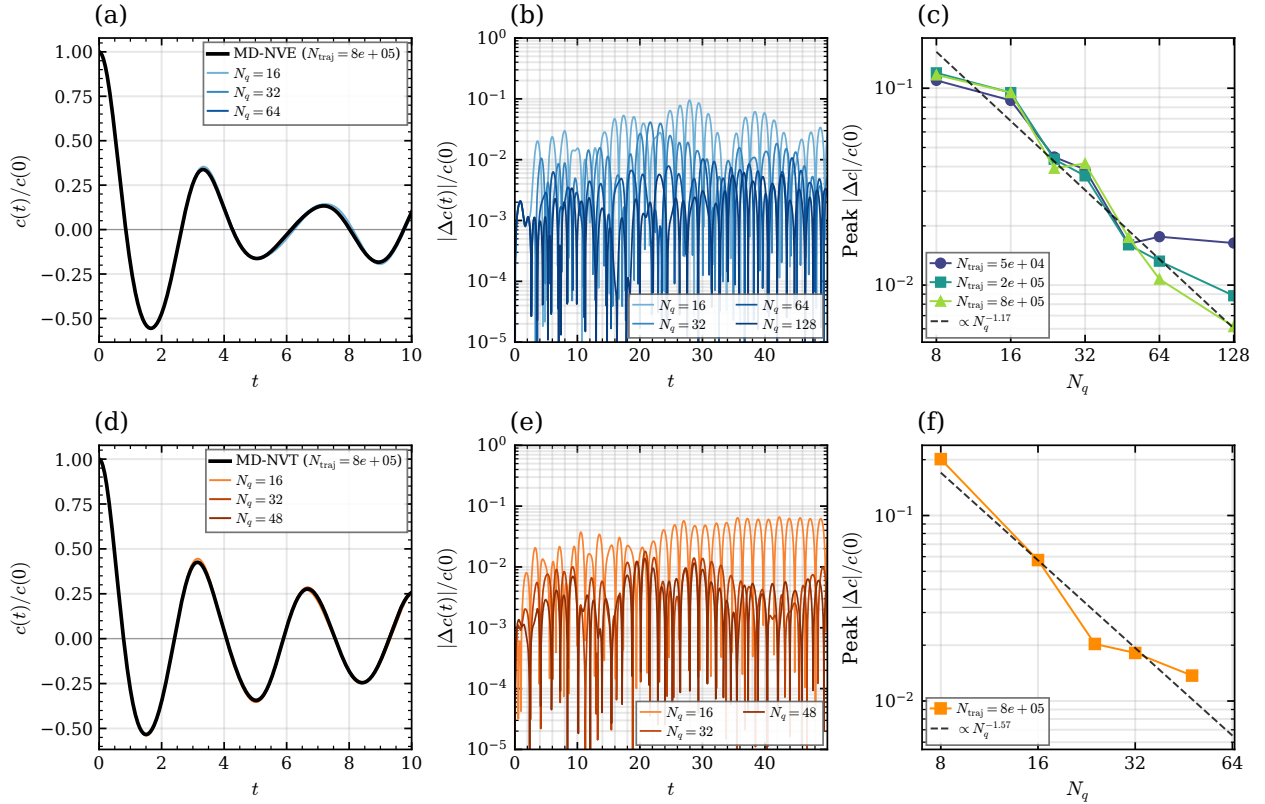


FIG. 3. **VACF convergence and finite-grid effects in the two-particle coupled cosine system.** The upper and lower rows show the NVE and Nosé–Hoover NVT results, respectively. The system is defined by Eq. (67) with  $V_0 = 5$ ,  $\varepsilon = 1.2$ ,  $m = T_0 = 1$ , and  $N_p = 64$ . The left column shows the short-time VACF, the middle column shows the deviation  $|\Delta c(t)|/c(0)$  from the MD reference, and the right column shows the peak deviation as a function of  $N_q$ . The peak deviation decreases empirically as approximately  $N_q^{-1.17}$  for NVE and  $N_q^{-1.57}$  for NVT. These exponents are empirical fits for this validation system and should not be interpreted as universal exponents.

points  $N_z$  appears as exponential error reduction with respect to the register size  $n_z$ . At the level of grid representation, this means that increasing the register by one qubit doubles the resolution along that axis, whereas a corresponding classical grid representation must explicitly store the doubled number of grid points.

Thus, the KvN inner product of the velocity-weighted state gives the normalized VACF for the selected dynamics  $\mathcal{D}$ . The finite-grid error in  $C_{vv}(t)$  decreases approximately as  $N_z^{-\gamma}$  over the observation range, and using a quantum register with  $N_z = 2^{n_z}$  translates this grid convergence into an exponential decrease with the number of qubits assigned to that axis. In the next section, we introduce the procedure for reading out this correlation function as a Green–Kubo integral.

## V. QPE BIN-ZERO READOUT OF GREEN–KUBO INTEGRALS

In the preceding section, we showed that the auto-correlation of a flux-excited KvN state gives the normalized time-correlation function associated with the se-

lected dynamics  $\mathcal{D}$ . In this section, we use this flux-excited state as the input to quantum phase estimation (QPE) and show that the bin-zero probability  $P_0$  of the ancilla register exactly yields a finite-window Bartlett-weighted Green–Kubo estimator. In Fig. 4, we validate the Bartlett-windowed Green–Kubo estimator obtained from the QPE bin-zero readout for both NVE dynamics and Nosé–Hoover-type NVT dynamics.

### A. Green–Kubo Formula and the Flux-Excited State

We now apply the KvN inner-product representation of Sec. IV B to the Green–Kubo formula. For a scalar flux  $J(\mathbf{z}_{\mathcal{D}})$  under the selected dynamics  $\mathcal{D} \in \{\text{NVE}, \text{NVT}\}$ , the equilibrium flux autocorrelation function is

$$C_{JJ}^{\mathcal{D}}(t) = \langle J(t)J(0) \rangle_{\text{eq}, \mathcal{D}}. \quad (74)$$

Here,  $J$  is understood as a mean-subtracted flux when its equilibrium mean is nonzero. The corresponding multiplication operator is  $\hat{J} = J(\hat{\mathbf{z}}_{\mathcal{D}})$ , and the normalized

flux-excited KvN state is

$$|\alpha_{\mathcal{D},J}\rangle = \frac{\hat{J}|\psi_{\text{eq},\mathcal{D}}\rangle}{\sqrt{C_{JJ}^{\mathcal{D}}(0)}}, \quad C_{JJ}^{\mathcal{D}}(0) = \langle \psi_{\text{eq},\mathcal{D}} | \hat{J}^2 | \psi_{\text{eq},\mathcal{D}} \rangle. \quad (75)$$

The normalized correlation function is then evaluated using the overlap representation derived in Eq. (66).

For the diffusion coefficient considered in this work, the flux is one velocity component. For the  $\ell$ th scalar degree of freedom,

$$J(\mathbf{z}_{\mathcal{D}}) = v_{\ell}(\mathbf{z}_{\mathcal{D}}) = \frac{p_{\ell}}{m_{\ell}}, \quad \hat{J} = \hat{v}_{\ell} = \frac{\hat{p}_{\ell}}{m_{\ell}}. \quad (76)$$

Therefore,

$$C_{JJ}^{\mathcal{D}}(t) = C_{vv,\ell}^{\mathcal{D}}(t), \quad C_{JJ}^{\mathcal{D}}(0) = C_{vv,\ell}^{\mathcal{D}}(0). \quad (77)$$

For a canonical distribution, the zero-time value is

$$C_{vv,\ell}^{\mathcal{D}}(0) = \frac{T_0}{m_{\ell}}. \quad (78)$$

The one-dimensional diffusion coefficient associated with this component is

$$D_{\mathcal{D}} = \int_0^{\infty} C_{vv,\ell}^{\mathcal{D}}(t) dt. \quad (79)$$

We use  $\mathcal{D} = \text{NVE}$  for Hamiltonian production dynamics and  $\mathcal{D} = \text{NVT}$  when the correlation function of the thermostatted dynamics itself is considered.

### B. QPE Bin-Zero Probability and the Bartlett Window

The one-step propagator used in QPE is

$$U_{\mathcal{D}} = U_{\mathcal{D}}(\Delta t), \quad (80)$$

where  $\Delta t$  is the discrete time step. The system register is initialized in the flux-excited state  $|\alpha_{\mathcal{D},J}\rangle$  defined in Eq. (75). With  $m_{\text{anc}}$  ancilla qubits, the number of QPE time samples is

$$K = 2^{m_{\text{anc}}}, \quad r = 0, 1, \dots, K-1. \quad (81)$$

QPE combines the powers  $U_{\mathcal{D}}^r$  through controlled applications of  $U_{\mathcal{D}}^{2^j}$ . The corresponding finite time window is

$$\tau_{\text{QPE}} = K\Delta t = 2^{m_{\text{anc}}} \Delta t. \quad (82)$$

In this subsection,  $P_0$  denotes the probability that the  $m_{\text{anc}}$ -qubit QPE ancilla register is measured in the zero bin, namely in the all-zero computational-basis state  $|0\rangle^{\otimes m_{\text{anc}}}$ , when the system register is initialized in  $|\alpha_{\mathcal{D},J}\rangle$  and the controlled unitary is  $U_{\mathcal{D}}$ .

The largest sampled time is  $(K-1)\Delta t$ , while the Bartlett window below vanishes at  $K\Delta t$ . The frequency resolution near zero phase is therefore estimated as

$$\delta\omega \sim \frac{2\pi}{\tau_{\text{QPE}}}. \quad (83)$$

Increasing  $m_{\text{anc}}$  improves this resolution, but also increases the largest controlled power of  $U_{\mathcal{D}}$ .

We denote the eigenstates and eigenphases of  $U_{\mathcal{D}}$  by  $|\phi_k\rangle$  and  $\theta_k$ , respectively:

$$U_{\mathcal{D}}|\phi_k\rangle = e^{-i\theta_k}|\phi_k\rangle. \quad (84)$$

The input state is expanded in this eigenbasis as

$$|\alpha_{\mathcal{D},J}\rangle = \sum_k a_k |\phi_k\rangle, \quad a_k = \langle \phi_k | \alpha_{\mathcal{D},J} \rangle. \quad (85)$$

Here,  $a_k$  is the expansion coefficient of the flux-excited state in the eigenbasis of  $U_{\mathcal{D}}$ . Standard QPE gives the zero-bin probability as

$$P_0 = \sum_k |a_k|^2 \left| \frac{1}{K} \sum_{r=0}^{K-1} e^{-ir\theta_k} \right|^2. \quad (86)$$

This is the eigenphase distribution of  $|\alpha_{\mathcal{D},J}\rangle$  averaged around zero phase by the Fejér kernel.

Using the squared-Dirichlet-kernel identity

$$\left| \sum_{r=0}^{K-1} e^{-ir\theta} \right|^2 = K + 2 \sum_{s=1}^{K-1} (K-s) \cos(s\theta), \quad (87)$$

and the normalized correlation function

$$c_{JJ}^{\mathcal{D}}(s\Delta t) = \text{Re} \langle \alpha_{\mathcal{D},J} | U_{\mathcal{D}}^s | \alpha_{\mathcal{D},J} \rangle, \quad (88)$$

we obtain

$$P_0 = \frac{1}{K^2} \left[ K + 2 \sum_{s=1}^{K-1} (K-s) c_{JJ}^{\mathcal{D}}(s\Delta t) \right]. \quad (89)$$

Equation (87) follows from the self-convolution of a finite geometric series; the derivation is given in Appendix B.

Multiplying Eq. (89) by  $C_{JJ}^{\mathcal{D}}(0)\tau_{\text{QPE}}/2$  gives the Bartlett-windowed Green-Kubo integral

$$\begin{aligned} \mathcal{I}_{\text{Bart}}^{\mathcal{D},J}(K) &\equiv \frac{1}{2} C_{JJ}^{\mathcal{D}}(0) \tau_{\text{QPE}} P_0 \\ &= C_{JJ}^{\mathcal{D}}(0) \Delta t \left[ \frac{1}{2} + \sum_{s=1}^{K-1} \left( 1 - \frac{s}{K} \right) c_{JJ}^{\mathcal{D}}(s\Delta t) \right]. \end{aligned} \quad (90)$$

The factor

$$w_s = 1 - \frac{s}{K}, \quad s = 0, 1, \dots, K, \quad (91)$$

is the triangular Bartlett window. It vanishes at  $s = K$ , and the coefficient of the  $s = 0$  term is  $1/2$ . Omitting this

endpoint coefficient breaks the correspondence with the QPE zero-bin probability and leaves an  $\mathcal{O}(\Delta t)$  systematic offset.

For diffusion,  $J = v_\ell$  and  $C_{JJ}^D(t) = C_{vv,\ell}^D(t)$ . The estimator used in this work is therefore

$$D_{\text{Bart}}^{\mathcal{D},\ell}(K) = \frac{1}{2} C_{vv,\ell}^D(0) \tau_{\text{QPE}} P_0, \quad \tau_{\text{QPE}} = 2^{m_{\text{anc}}} \Delta t. \quad (92)$$

Thus, the QPE readout does not require reconstructing the full phase distribution. It is sufficient to estimate the zero-bin probability  $P_0$  for the QPE circuit initialized with the velocity-excited state.

### C. Finite-Time Window and Finite-Grid Error

Equation (92) gives the exact finite-window Bartlett estimator associated with the QPE time window  $\tau_{\text{QPE}}$ . To recover the physical diffusion coefficient  $D_{\mathcal{D}}$ , the window length must be long compared with the decay time of the velocity autocorrelation function. In continuous time, the corresponding Bartlett-windowed integral is

$$D_{\text{Bart}}^{\mathcal{D},\ell}(\tau) \simeq \int_0^\tau \left(1 - \frac{t}{\tau}\right) C_{vv,\ell}^D(t) dt. \quad (93)$$

The window factor suppresses spectral leakage, but at finite  $\tau$  it also attenuates long-time components of the correlation function. Therefore,  $D_{\text{Bart}}^{\mathcal{D},\ell}(\tau)$  retains a finite-window bias. When  $C_{vv,\ell}^D(t)$  decays sufficiently rapidly and  $\tau$  exceeds the dominant correlation time, the leading correction is expected to scale as  $1/\tau$ , or equivalently as  $1/K$ . We model the convergence regime as

$$D_{\text{Bart}}^{\mathcal{D},\ell}(K) = D_\infty^{\mathcal{D},\ell} + \frac{a_1}{K} + \mathcal{O}(K^{-2}), \quad (94)$$

and estimate  $D_\infty^{\mathcal{D},\ell}$  by extrapolation in  $1/K$ .

In Sec. IV D, the finite-grid error of the correlation function within a fixed observation window was found to decrease approximately as  $N_z^{-\gamma}$ . This error propagates linearly to the Bartlett estimator. We denote by  $c_{vv,\ell}^{\mathcal{D},\text{disc}}(t)$  the normalized VACF obtained from the finite-grid discrete KvN calculation, and by  $c_{vv,\ell}^{\mathcal{D},\text{cont}}(t)$  the corresponding normalized VACF of the continuum dynamics. At the discrete time  $t = s\Delta t$ , define

$$\Delta c_s = c_{vv,\ell}^{\mathcal{D},\text{disc}}(s\Delta t) - c_{vv,\ell}^{\mathcal{D},\text{cont}}(s\Delta t). \quad (95)$$

If  $|\Delta c_s| \leq \epsilon_c$  for  $s = 0, 1, \dots, K-1$ , then Eq. (90) gives

$$\begin{aligned} |\Delta D_{\text{Bart}}^{\mathcal{D},\ell}| &\leq C_{vv,\ell}^D(0) \Delta t \left[ \frac{1}{2} + \sum_{s=1}^{K-1} \left(1 - \frac{s}{K}\right) \right] \epsilon_c \\ &= \frac{1}{2} C_{vv,\ell}^D(0) \tau_{\text{QPE}} \epsilon_c. \end{aligned} \quad (96)$$

This estimate gives the accuracy required for the normalized correlation function to achieve a target error in

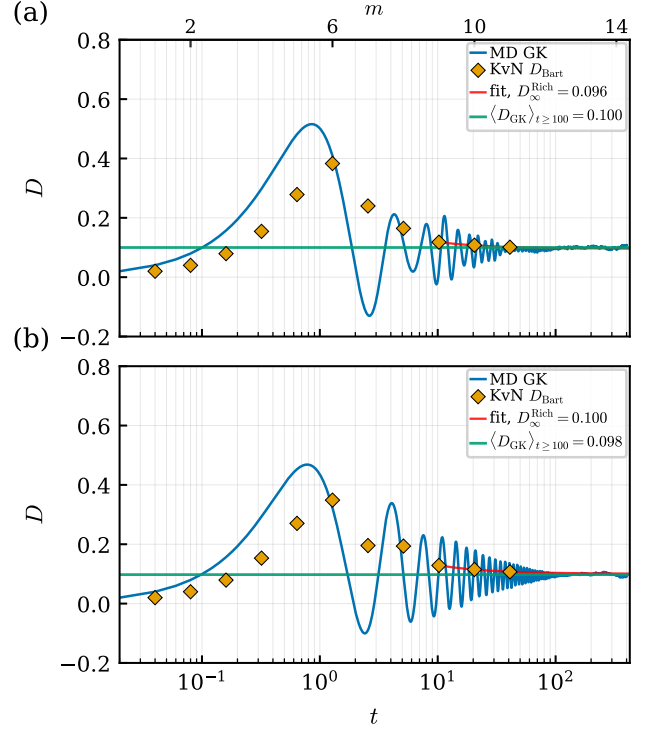


FIG. 4. **Comparison between the Green-Kubo integral and the KvN Bartlett estimator.** (a) NVE dynamics with  $N_q = 128$ . (b) Nosé-Hoover-type NVT dynamics with  $N_q = 48$ . The blue curve shows the cumulative Green-Kubo integral  $D_{\text{GK}}(t) = \int_0^t C_{vv}(t') dt'$  obtained from the classical MD velocity autocorrelation function, while the yellow diamonds show the KvN Bartlett estimator  $D_{\text{Bart}}(m_{\text{anc}})$ . The lower axis gives the physical time  $t$ , and the upper axis gives  $m = \log_2(t/\Delta t)$ . The red line shows a first-order extrapolation in  $1/K$  using the  $m = 9, 10, 11$  points, and the green line shows the classical long-time reference  $\langle D_{\text{GK}} \rangle_{100 \leq t \leq 400}$ .

$D_{\text{Bart}}^{\mathcal{D},\ell}$ . Together with Eq. (73), it also estimates the number of grid qubits when the grid size is written as  $N_z = 2^{n_z}$ .

The systematic error in  $D_{\text{Bart}}^{\mathcal{D},\ell}$  mainly consists of finite-grid error, Trotter error, and finite-window bias. The statistical error from estimating  $P_0$  with a finite number of shots is treated separately in the circuit-validation and amplitude-estimation analyses. In particular, MLAE is introduced to improve the query scaling for estimating  $P_0$  relative to direct shot sampling.

### D. Numerical Validation for the Two-Particle Coupled Cosine System

Figure 4 shows a numerical validation of the QPE bin-zero readout for the two-particle coupled cosine system. We apply the same readout formula to both NVE dynamics and Nosé-Hoover-type NVT dynamics. The blue curve is the finite-time Green-Kubo integral  $D_{\text{GK}}(t)$ , ob-

tained by directly integrating the velocity autocorrelation function from classical MD. The yellow diamonds are  $D_{\text{Bart}}(m_{\text{anc}})$ , computed from KvN state-vector propagation. By Eq. (92), each marker is the bin-zero readout value that would be returned, in the infinite-shot limit, by a QPE circuit using the corresponding  $U_{\mathcal{D}}(\Delta t)$  and flux-excited state  $|\alpha_{\mathcal{D}}\rangle$ .

The finite- $m_{\text{anc}}$  value  $D_{\text{Bart}}(m_{\text{anc}})$  is not simply the finite-time Green–Kubo integral sampled at  $t = \tau_{\text{QPE}} = 2^{m_{\text{anc}}}\Delta t$ . As shown in Eq. (90), it is a discrete integral of the correlation function over  $0 \leq t \leq \tau_{\text{QPE}}$ , multiplied by the Bartlett window. Because the correlation function in the present system contains oscillatory components, a large transient peak appears for short window lengths, and the estimator returns toward its long-time value as  $m_{\text{anc}}$  increases. This nonmonotonic behavior is not a failure of QPE, but a feature of the finite-window Bartlett estimator.

The classical finite-time Green–Kubo integral does not become perfectly constant for finite trajectory lengths. We therefore use the average of  $D_{\text{GK}}(t)$  over the interval  $100 \leq t \leq 400$  as the classical long-time reference. For NVE, we obtain

$$\langle D_{\text{GK}}^{\text{NVE}} \rangle_{100 \leq t \leq 400} = 0.1000 \pm 0.0035, \quad (97)$$

and a first-order extrapolation in  $1/K$  using the  $D_{\text{Bart}}(m)$  values at  $m = 9, 10, 11$  gives

$$D_{\infty, \text{NVE}}^{\text{Rich}} = 0.0960 \pm 0.0012. \quad (98)$$

For NVT, the same analysis gives

$$\langle D_{\text{GK}}^{\text{NVT}} \rangle_{100 \leq t \leq 400} = 0.0976 \pm 0.0043, \quad (99)$$

$$D_{\infty, \text{NVT}}^{\text{Rich}} = 0.1004 \pm 0.0006. \quad (100)$$

The uncertainties quoted here are either the fluctuations of the classical MD running integral within the long-time window or the standard errors of the Richardson extrapolation. For both dynamics, the extrapolated KvN Bartlett estimator agrees with the long-time Green–Kubo reference from classical MD within a few percent.

This comparison verifies two points. First, the QPE bin-zero probability obtained from the flux-excited state returns the Bartlett-windowed Green–Kubo estimator defined by Eq. (92). Second, in the regime where the finite-window bias is well described by the leading  $1/K$  correction, extrapolating  $D_{\text{Bart}}(m_{\text{anc}})$  in  $1/K$  gives a value consistent with the long-time Green–Kubo integral from classical MD. The remaining accuracy is controlled by finite-window extrapolation, finite-grid error, Trotter error, and the statistical error of the classical reference.

In summary, the quantum readout of the Green–Kubo integral proceeds as follows. The correlation function is represented as the autocorrelation of the flux-excited state  $|\alpha_{\mathcal{D}}\rangle$  under the KvN propagator  $U_{\mathcal{D}}$ . Supplying this state to QPE gives a bin-zero probability  $P_0$ , which corresponds to the discrete Green–Kubo integral multiplied by a Bartlett window. The resulting finite- $K$  bias can be corrected by a  $1/K$  extrapolation in the convergence regime.

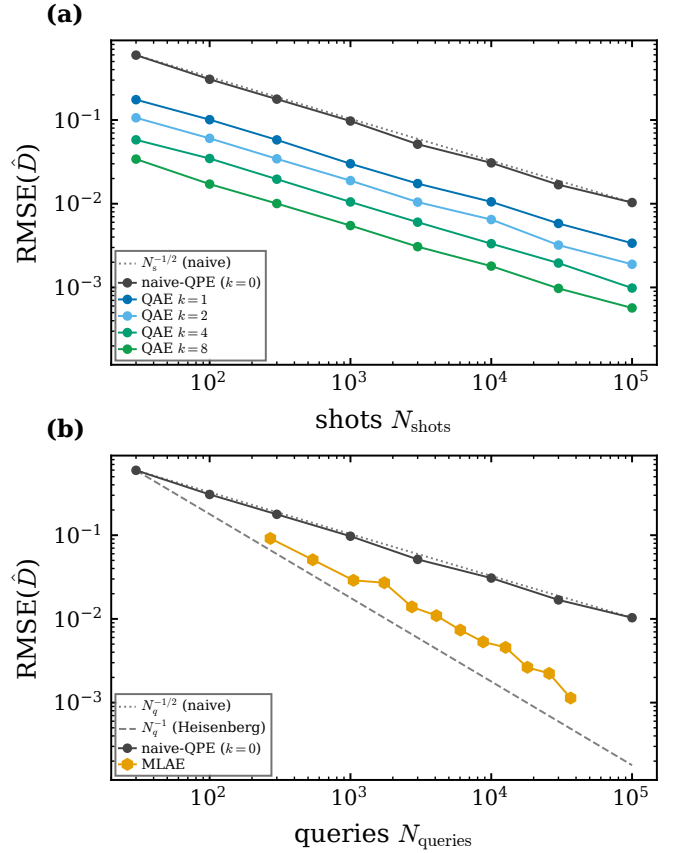


FIG. 5. **RMSE reduction by amplitude estimation for the QPE bin-zero readout.** The calculation uses the two-particle coupled cosine system with an 8-qubit system register and  $m_{\text{anc}} = 12$  QPE ancilla qubits. The parameters are  $K = 2^{12}$ ,  $\Delta t = 0.02$ ,  $\tau_{\text{QPE}} = 81.92$ ,  $C_{vv}(0) = 1.1334$ , and  $P_0^{\text{exact}} = 4.097 \times 10^{-3}$ ; the state-vector reference is  $D_{\text{Bart}} = 0.19020$ . (a) Prefactor reduction for fixed Grover powers  $k \in \{0, 1, 2, 4, 8\}$ . The horizontal axis is the number of shots  $N_{\text{shots}}$  used for each fixed- $k$  circuit, and the vertical axis is the RMSE of  $\hat{D}$  over  $N_{\text{seeds}} = 1000$  Monte Carlo seeds. All series follow  $N_{\text{shots}}^{-1/2}$  scaling, while the prefactor decreases as  $k$  increases. (b) Query-count dependence of growing-schedule MLAE based on the EIS. The horizontal axis is  $N_{\text{queries}} = \sum_{\ell} N_{\ell}(2k_{\ell} + 1)$ , and the vertical axis is the same RMSE. Naive QPE follows  $N_{\text{queries}}^{-1/2}$  scaling, whereas the late-stage MLAE data have a fitted slope of  $-0.953$ , close to  $N_{\text{queries}}^{-1}$ .

## VI. QUADRATIC SPEEDUP IN $P_0$ ESTIMATION VIA AMPLITUDE ESTIMATION

In Sec. V, we showed that the flux-excited state  $|\alpha_{\mathcal{D}}\rangle$ , together with the KvN propagator  $U = S_2^{\mathcal{D}}(\Delta t)$ , maps the Bartlett-windowed Green–Kubo estimator to the QPE bin-zero probability  $P_0$ . In this section, we use amplitude estimation instead of direct shot sampling to estimate  $P_0$ . For the fixed QPE oracle defining  $P_0$ , this improves the query complexity of statistical estimation from  $O(\epsilon^{-2})$  to  $O(\epsilon^{-1})$ .

### A. Statistical Error of Direct Sampling

Let  $P_0$  be the probability of obtaining bin zero in the ancilla measurement of an  $m_{\text{anc}}$ -qubit QPE circuit. If the QPE circuit is executed  $N_{\text{shots}}$  times and bin zero is observed  $N_0$  times, the direct-sampling estimator is

$$\hat{P}_0 = \frac{N_0}{N_{\text{shots}}}. \quad (101)$$

Each shot is a Bernoulli trial, and hence

$$\text{Var}(\hat{P}_0) = \frac{P_0(1 - P_0)}{N_{\text{shots}}}. \quad (102)$$

This fluctuation propagates to the statistical error of  $\hat{D}$  through

$$\hat{D} = \frac{1}{2}C_{JJ}^{(\mathcal{D})}(0)\tau_{\text{QPE}}\hat{P}_0. \quad (103)$$

For  $J = v$ , Eq. (103) is the velocity-autocorrelation readout formula for the diffusion coefficient.

To estimate  $P_0$  with relative error  $\epsilon_{\text{rel}}$ , Eq. (102) gives, approximately,

$$N_{\text{shots}} \simeq \frac{1 - P_0}{\epsilon_{\text{rel}}^2 P_0}. \quad (104)$$

For  $P_0 \ll 1$ , the required number of shots grows in proportion to  $1/P_0$ . This is the statistical bottleneck that arises in the readout stage of the QPE bin-zero method.

### B. Oracle Structure for Amplitude Estimation

We regard the full QPE circuit as a single unitary  $A$ . This unitary includes preparation of the flux-excited state  $|\alpha_{\mathcal{D}}\rangle$ , the controlled- $U^{2^j}$  operations, and the inverse QFT on the ancilla register. Defining the ancilla bin-zero subspace as the good subspace, we can write

$$A|0\rangle = \sqrt{P_0}|\Psi_{\text{good}}\rangle + \sqrt{1 - P_0}|\Psi_{\text{bad}}\rangle. \quad (105)$$

Here  $|0\rangle$  denotes the all-zero input to the state-preparation and QPE circuit,  $|\Psi_{\text{good}}\rangle$  is the normalized state projected onto the ancilla bin-zero subspace, and  $|\Psi_{\text{bad}}\rangle$  belongs to the orthogonal complement. We define the amplitude angle  $\theta$  by

$$P_0 = \sin^2 \theta. \quad (106)$$

Standard amplitude amplification constructs the Grover iterate

$$Q = -AS_0A^\dagger S_\chi \quad (107)$$

from the reflection  $S_\chi$  about the good subspace and the reflection  $S_0$  about the all-zero input state [16]. After applying  $Q^k A$  to  $|0\rangle$ , the probability of observing a good outcome is

$$p_k(\theta) = \sin^2 [(2k + 1)\theta]. \quad (108)$$

For small  $P_0$ , one has  $\theta \simeq \sqrt{P_0}$ . The Grover power  $k$  therefore magnifies the amplitude angle by a factor  $2k + 1$  before measurement.

### C. Prefactor Reduction with a Fixed Grover Power

We first consider the case in which a single Grover power  $k$  is fixed. At a fixed  $k$ , the measurement outcome is still a Bernoulli random variable, and the RMSE therefore retains the same  $N_{\text{shots}}^{-1/2}$  scaling as direct sampling. The effect of amplitude amplification appears instead in the prefactor.

The Fisher information per shot of the Bernoulli distribution  $p_k(\theta)$ , with respect to the amplitude angle  $\theta$ , is

$$I_k(\theta) = \frac{1}{p_k(1 - p_k)} \left( \frac{\partial p_k}{\partial \theta} \right)^2 = 4(2k + 1)^2. \quad (109)$$

Thus, on a branch where the Grover oscillation is not folded and  $\theta$  can be recovered uniquely, the measured probability  $\hat{p}_k$  can be inverted as

$$\hat{\theta} = \frac{1}{2k + 1} \arcsin \sqrt{\hat{p}_k}. \quad (110)$$

This gives

$$\sigma(\hat{\theta}) \simeq \frac{1}{2(2k + 1)\sqrt{N_{\text{shots}}}}. \quad (111)$$

Propagating this error to  $\hat{D} = (1/2)C_{vv}(0)\tau_{\text{QPE}}\sin^2 \hat{\theta}$  yields

$$\sigma(\hat{D}) \simeq \frac{C_{vv}(0)\tau_{\text{QPE}} \sin \theta \cos \theta}{2(2k + 1)\sqrt{N_{\text{shots}}}}. \quad (112)$$

Therefore, amplitude amplification with a fixed  $k$  can reduce the RMSE prefactor by approximately a factor of  $2k + 1$ , while leaving the  $N_{\text{shots}}^{-1/2}$  scaling unchanged.

The RMSE in Fig. 5(a) is defined using the state-vector value of  $D_{\text{Bart}}$  as the reference. Specifically, for each  $k \in \{0, 1, 2, 4, 8\}$ , each shot number  $N_{\text{shots}}$ , and each Monte Carlo seed  $s = 1, \dots, N_{\text{seeds}}$ , we estimate  $\hat{\theta}^{(s)}$  from the measurement outcome using Eq. (110). We then compute

$$\hat{P}_0^{(s)} = \sin^2 \hat{\theta}^{(s)}, \quad \hat{D}^{(s)} = \frac{1}{2}C_{vv}(0)\tau_{\text{QPE}}\hat{P}_0^{(s)}, \quad (113)$$

and evaluate

$$\text{RMSE}(\hat{D}) = \sqrt{\frac{1}{N_{\text{seeds}}} \sum_{s=1}^{N_{\text{seeds}}} \left( \hat{D}^{(s)} - D_{\text{Bart}} \right)^2}. \quad (114)$$

In the present calculation,  $N_{\text{seeds}} = 1000$ . The reference value  $D_{\text{Bart}}$  is the Bartlett estimator for the QPE window with  $m_{\text{anc}} = 12$ .

The fixed- $k$  method reduces the prefactor for estimating  $P_0$  at a single circuit depth. However, if  $k$  is made too large, the periodicity of  $\sin^2[(2k + 1)\theta]$  makes the estimate of  $\theta$  nonunique. To avoid this branch ambiguity, one must combine measurements at multiple Grover powers.

### D. Heisenberg-Type Scaling with MLAE

In maximum-likelihood amplitude estimation (MLAE), circuits  $Q^{k_\ell}A$  are executed for multiple Grover powers  $\{k_\ell\}$ , and all measurement outcomes are combined into a single likelihood function [17]. If  $h_\ell$  good outcomes are obtained out of  $N_\ell$  shots, the likelihood is

$$\mathcal{L}(\theta) = \prod_{\ell} [p_{k_\ell}(\theta)]^{h_\ell} [1 - p_{k_\ell}(\theta)]^{N_\ell - h_\ell}, \quad (115)$$

where  $p_{k_\ell}(\theta) = \sin^2[(2k_\ell + 1)\theta]$ . From the maximum-likelihood estimate  $\hat{\theta}$ , we obtain  $\hat{P}_0 = \sin^2 \hat{\theta}$  and reconstruct  $\hat{D}$  using Eq. (103).

Following the Exponential Incremental Sequence (EIS) of Suzuki *et al.* [17], we use a hierarchical schedule in which the set of Grover powers is enlarged step by step. In the EIS, the measurement magnification factor  $M_\ell = 2k_\ell + 1$ , denoted by  $m_\ell$  in the notation of Suzuki *et al.*, increases approximately as  $M_\ell \sim 2^{\ell-1}$ . We implement this sequence as nested sets  $\mathcal{K}^{(L)} = \{k_\ell\}_{\ell=1}^L$  satisfying  $\mathcal{K}^{(L+1)} \supset \mathcal{K}^{(L)}$ , and refer to this nested structure as a *growing schedule*. Figure 5(b) uses this growing schedule. For each  $k_\ell$ , we use only  $N_\ell = 30$  shots and evaluate the RMSE in Eq. (114) over  $N_{\text{seeds}} = 1000$  Monte Carlo seeds. Since the circuit with Grover power  $k_\ell$  contains  $A$  a total of  $2k_\ell + 1$  times, we define the total query count as

$$N_{\text{queries}} = \sum_{\ell} N_\ell (2k_\ell + 1). \quad (116)$$

For direct sampling, the RMSE decreases as  $N_{\text{queries}}^{-1/2}$ . In contrast, MLAE with the growing schedule can approach  $N_{\text{queries}}^{-1}$  scaling. This is the standard quadratic improvement of amplitude estimation, and iterative amplitude estimation achieves the same query-complexity improvement [18].

In Fig. 5(b), naive QPE follows the  $N_{\text{queries}}^{-1/2}$  slope, whereas the late-stage MLAE data give a log-log regression slope of  $-0.953$ . At the final stage,  $N_{\text{queries}} = 36600$  and  $\text{RMSE} \simeq 1.02 \times 10^{-3}$ , and  $\text{RMSE} \times N_{\text{queries}}$  remains nearly constant. This behavior is consistent with near-Heisenberg  $N_{\text{queries}}^{-1}$  scaling in the numerical regime studied here. Thus, for the task of estimating  $P_0$  defined by the same QPE oracle, amplitude estimation provides a quadratic query-complexity advantage over direct shot sampling.

## VII. RESOURCE ANALYSIS

In this section, we summarize the gate costs of the KvN circuits constructed in Sec. III. Our aim is to compare the NVE and NVT implementations on the same footing and to identify which circuit components can be implemented with polynomial gate cost and which become bottlenecks

in the present construction. As a cost metric, we use the number of CX gates after transpiling the Qiskit circuits into the  $\{\text{CX}, u_3\}$  basis. The CX counts reported here are logical-level measures of circuit complexity and do not include hardware noise, routing overhead specific to a device topology, or error-correction overhead.

In the following, we denote the numbers of qubits in the position, momentum, and Nosé–Hoover variable registers by  $n_q$ ,  $n_p$ , and  $n_\xi$ , respectively. For NVE, the total register size is  $n = n_q + n_p$ , whereas for NVT it is  $n = n_q + n_p + n_\xi$ .

### A. Implementation Cost of the $\hat{H}_3$ Dilation Block

The main resource difference between NVT and NVE arises from the Nosé–Hoover friction term,

$$\hat{H}_3 = -\hat{\xi} \otimes \hat{D}_p, \quad \hat{D}_p = \frac{1}{2}(\hat{p}\hat{\lambda}_p + \hat{\lambda}_p\hat{p}). \quad (117)$$

This term is specific to the thermostat. Although  $\hat{D}_p$  is the generator of momentum-space dilations in the continuum limit, a quantum circuit must implement a finite-dimensional representation of it on a discretized momentum grid. In this work, we discretize the derivative along the  $p$  axis by a centered difference and decompose the resulting finite-dimensional matrix into a real linear combination of Pauli strings. We refer to this implementation as the centered-difference Pauli-decomposition method.

The operator  $\hat{D}_p$  obtained from the centered difference has a nearest-neighbor finite-difference structure. However, after binary encoding of the  $p$  register, the number of Pauli strings grows with the number of momentum grid points,  $N_p = 2^{n_p}$ . The centered-difference Pauli-decomposition results in Fig. 6 are based on representing the derivative operator  $\hat{D}_p$  by a cyclic central-difference matrix with periodic boundary conditions. Expanding this matrix in the Pauli basis on  $n_p$  qubits gives a set of nonzero Pauli terms whose cardinality we denote by  $N_{D_p}^{\text{cyc}}(n_p)$ . We also define  $W_{D_p}^{\text{cyc}}(n_p)$  as the corresponding weighted Pauli sum, obtained by summing the implementation weights associated with the individual Pauli-string lengths. This gives

$$N_{D_p}^{\text{cyc}}(n_p) = \frac{7}{4}2^{n_p} - (n_p + 2), \quad (118)$$

$$W_{D_p}^{\text{cyc}}(n_p) = \frac{7}{4}n_p 2^{n_p} - 3 \cdot 2^{n_p} + 3. \quad (119)$$

The coordinate operator  $\hat{\xi}$  is diagonal on the  $\xi$  register and can be expanded in Pauli- $Z$  strings on  $n_\xi$  qubits. Therefore, the Pauli-evolution cost of  $\hat{H}_3$  is approximately proportional to  $n_\xi W_{D_p}^{\text{cyc}}(n_p)$ . For the centered-difference Pauli-decomposition method, this gives

$$N_{\text{CX}}(e^{-i\delta t \hat{H}_3}) = \mathcal{O}(n_\xi n_p 2^{n_p}). \quad (120)$$

Equivalently, since  $N_p = 2^{n_p}$ , this scaling is quasi-linear in the number of momentum grid points,  $\mathcal{O}(n_\xi N_p \log N_p)$ ,

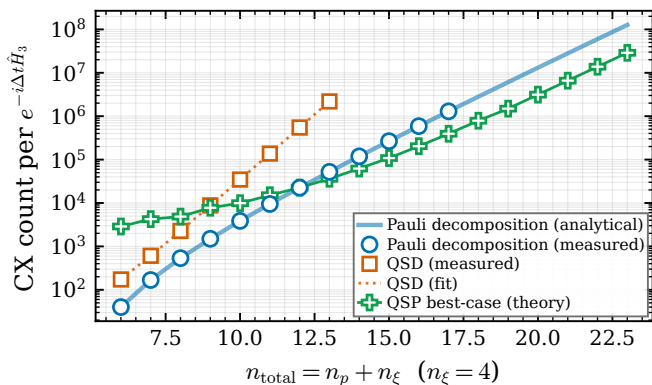


FIG. 6. **CX cost of the  $\hat{H}_3$  dilation block.** The horizontal axis is  $n_{\text{total}} = n_p + n_\xi$ , with  $n_\xi = 4$  fixed. The blue solid line is the analytic prediction for the centered-difference Pauli-decomposition method and follows the same  $n_p 2^{n_p}$ -type growth as the weighted Pauli sum in Eq. (119). The blue circles are the CX counts obtained by transpiling the corresponding Pauli-evolution circuits in Qiskit. The orange squares are the CX counts obtained by treating  $e^{-i\delta t \hat{H}_3}$  as a generic dense unitary and synthesizing it by quantum Shannon decomposition (QSD). The orange dotted line is a fit of the form  $c_1 4^{n_{\text{total}}}$ , representing the cost of generic unitary synthesis without exploiting the structure of  $\hat{H}_3$ . The green points show a best-case theoretical reference based on QSP Hamiltonian simulation, assuming that the sparse-access oracles described in the text are available at low cost.

and therefore exponential in the number of momentum qubits  $n_p$ .

Figure 6 compares three estimates for implementing  $e^{-i\delta t \hat{H}_3}$ . The first is the centered-difference Pauli-decomposition method. The blue solid line gives the analytic prediction for centered-difference Pauli evolution, and the blue circles show the CX counts after Qiskit transpilation. Over the measured range, both exhibit the same  $n_p 2^{n_p}$ -type growth. Equation (119) gives the closed form of the weighted Pauli sum responsible for this scaling. This is the implementation used in the numerical circuits of the present work.

The second estimate is dense-unitary synthesis by QSD. Here, the matrix  $e^{-i\delta t \hat{H}_3}$  is treated as a generic  $2^{n_{\text{total}}} \times 2^{n_{\text{total}}}$  unitary, without using the sparsity or tensor-product structure of  $\hat{H}_3$ . Since the synthesis cost of a generic unitary scales as  $4^{n_{\text{total}}}$  [33], the orange dotted line in Fig. 6 has the same exponential form. The centered-difference Pauli-decomposition method lies below QSD because it explicitly exploits the nearest-neighbor finite-difference structure of  $\hat{D}_p$  through a Pauli-sum representation.

The third estimate is a best-case theoretical reference based on QSP [34, 35]. For this curve, we assume that a location oracle  $O_{\text{loc}}$  and a value oracle  $O_{\text{val}}$  for block encoding  $\hat{H}_3$  as a sparse Hamiltonian are available at low cost. Thus, the green points are not transpiled counts from an implemented circuit, but target values in the

sparse-access oracle model. Under this assumption, the QSP polynomial degree scales as  $K_{\text{QSP}} = O(2^{n_p})$ , and the leading CX scaling becomes  $\mathcal{O}(n_{\text{total}} 2^{n_p})$ . The evaluation method and oracle assumptions are summarized in Appendix D.

This comparison should be interpreted carefully. Figure 6 shows that the centered-difference Pauli-decomposition method is substantially less costly than structure-agnostic QSD for the sizes considered here. At the same time, it indicates that a different implementation route could become preferable if an efficient sparse block encoding of the friction term  $\hat{H}_3$  were available.

## B. One-Step Circuit Costs for NVE and NVT

Here, we distinguish the asymptotic scaling implied by the circuit construction from the benchmark implementation used for the explicit gate-count measurements. The general expressions are written for  $N_f$  classical degrees of freedom. By contrast, the explicit circuit syntheses in Figs. 7 and 8 use the one-dimensional single-particle cosine potential:

$$V(q) = V_0 \cos q, \quad F(q) = -\partial_q V(q) = V_0 \sin q. \quad (121)$$

The CX counts reported below are the values for the implementation of Eq. (121), while the scaling with register size follows from the construction of the individual circuit blocks.

The one-step NVE propagator is  $U_1(\Delta t/2)U_2(\Delta t)U_1(\Delta t/2)$  in Fig. 2(a). In  $U_1$ , the Fourier transform on the  $q$  register diagonalizes  $\hat{\lambda}_q$  as  $\hat{k}_q$ , and the phase  $\Phi_q(\delta t) = \exp[-i\delta t \hat{p} \hat{k}_q / m]$  is applied. In  $U_2$ , the Fourier transform on the  $p$  register maps  $\hat{\lambda}_p$  to  $\hat{k}_p$ , and the phase  $\Phi_p(\delta t) = \exp[-i\delta t F(\hat{q}) \hat{k}_p]$  is applied. For Eq. (121),  $F(\hat{q})$  is implemented as a diagonal function on the  $q$  register. Because these phases can be written as functions of the computational-basis values of the registers, they need not be synthesized as generic diagonal unitaries. The same structure is used in the split-operator quantum simulation of chemical dynamics by Kassal *et al.* and in the diagonal-unitary synthesis of Welch *et al.* [5, 26].

Fig. 7 shows the CX count of the NVE one-step circuit. The measured values are described by

$$N_{\text{CX}}^{\text{NVE}}(n) = 3n^2 + 2n - 21, \quad n = n_q + n_p. \quad (122)$$

As seen from the breakdown in Fig. 7(a), the QFT/IQFT blocks and the bilinear-phase components are all  $\mathcal{O}(n^2)$ . Therefore, the one-step implementation of NVE remains polynomial in the number of register qubits. This means that, while the circuit represents a grid with  $N_p = 2^{n_p}$  momentum points, the gate count can be kept polynomial in  $n_p$  rather than in  $N_p$ .

The one-step NVT propagator is  $U_1 U_2 U_3 U_4 U_3 U_2 U_1$  in Fig. 2(b). The blocks  $U_1$  and  $U_2$  are the same split-operator blocks as in NVE, and  $U_4$  is implemented as a

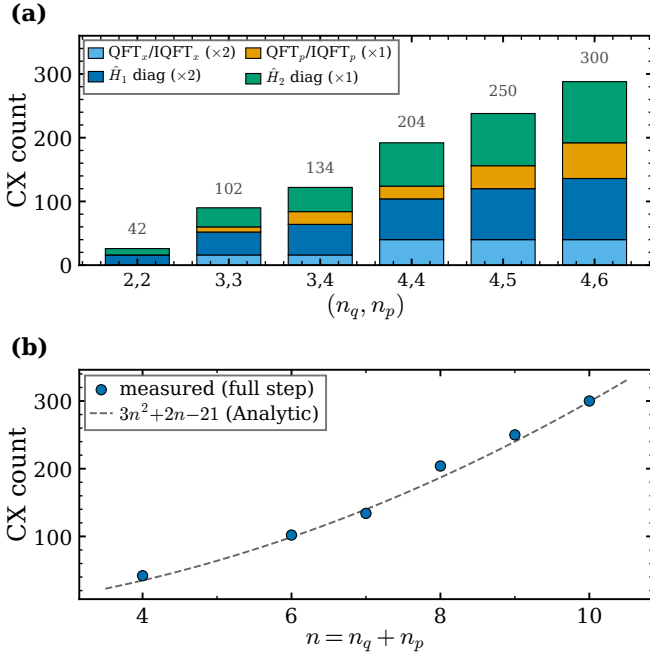


FIG. 7. **CX cost of the NVE one-step propagator.** (a) Component-wise breakdown. The contributions from  $\mathcal{F}_q$  and  $\mathcal{F}_p^\dagger$ , the bilinear phase of  $\hat{H}_1$ ,  $\mathcal{F}_p$  and  $\mathcal{F}_p^\dagger$ , and the diagonal phase of  $\hat{H}_2$  are shown separately. The  $n_x$  in the figure corresponds to  $n_q$  in the text. The explicit gate-count benchmark uses the one-dimensional single-particle cosine potential in Eq. (121). (b) Total CX count as a function of  $n = n_q + n_p$ . The measured values follow  $3n^2 + 2n - 21$ , showing that the NVE one-step circuit grows quadratically with the number of qubits.

diagonal phase by applying a Fourier transform to the  $\xi$  register,

$$\hat{H}_4 = \frac{(\hat{p}^2/m) - N_f T_0}{Q} \hat{\lambda}_\xi. \quad (123)$$

These blocks have polynomial cost. The newly dominant contribution in NVT is the twice-appearing block  $U_3(\Delta t/2) = \exp[-i(\Delta t/2)\hat{H}_3]$ .

Fig. 8 shows the cost of the NVT one-step circuit. The fits for  $n_\xi = 2, 3, 4$  are

$$\begin{aligned} N_{\text{CX}}^{\text{NVT}}|_{n_\xi=2} &\simeq 5.06 n_p 2^{n_p} + 11.2 2^{n_p} + 77, \\ N_{\text{CX}}^{\text{NVT}}|_{n_\xi=3} &\simeq 4.96 n_p 2^{n_p} + 19.2 2^{n_p} + 69, \\ N_{\text{CX}}^{\text{NVT}}|_{n_\xi=4} &\simeq 4.85 n_p 2^{n_p} + 27.2 2^{n_p} + 68. \end{aligned} \quad (124)$$

The leading terms are all proportional to  $n_p 2^{n_p}$ . The differences among the values of  $n_\xi$  appear in the constant factors originating from the Pauli-Z expansion of  $\hat{\xi}$  and in secondary terms introduced by the transpiler optimization. In general,

$$N_{\text{CX}}^{\text{NVT}} = \mathcal{O}(n_\xi n_p 2^{n_p}) \quad (125)$$

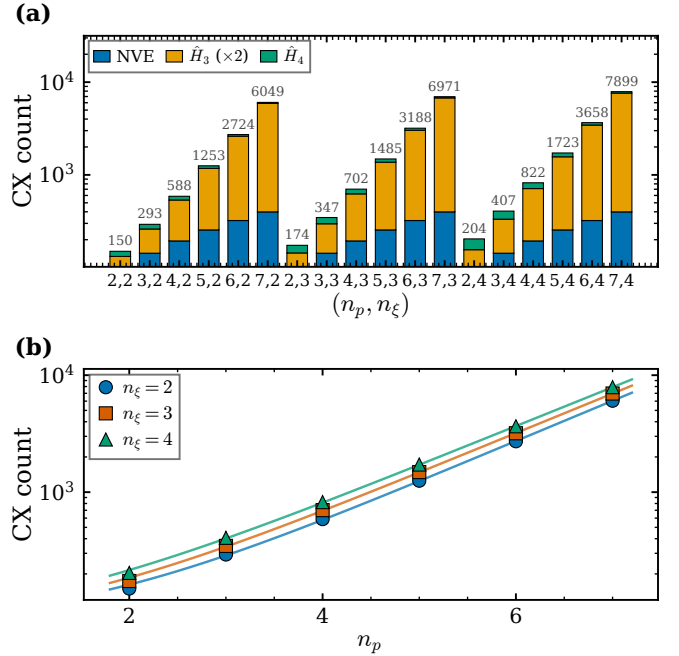


FIG. 8. **CX cost of the NVT one-step propagator.** (a) Stacked breakdown of the CX count. The split-operator part, which has the same form as in NVE, the two occurrences of the  $\hat{H}_3$  dilation block, and the thermostat block  $\hat{H}_4$  are shown separately. The explicit gate-count benchmark uses the one-dimensional single-particle cosine potential in Eq. (121). (b) Total CX count as a function of  $n_p$ . The series for  $n_\xi = 2, 3, 4$  follow fits of the form  $n_p 2^{n_p}$ . This reflects the  $n_p 2^{n_p}$ -type growth of the weighted Pauli sum in the centered-difference Pauli evolution.

and, in the range shown in the figure with fixed  $n_\xi$ , this can be read as  $\mathcal{O}(n_p 2^{n_p})$ .

Table I summarizes the scaling of the one-step propagators and the  $\hat{H}_3$  block. The first two rows compare the NVE and NVT one-step circuits constructed in the main text. These scalings are asymptotic estimates based on the construction of the circuit blocks, whereas the numerical CX counts in Figs. 7 and 8 were measured for the benchmark implementation in Eq. (121). The last three rows compare different methods for implementing the  $\hat{H}_3$  block, which is the dominant contribution in NVT. Here,  $n = n_q + n_p$  and  $n_{\text{total}} = n_p + n_\xi$ .

## VIII. CONCLUSION AND OUTLOOK

In this work, we formulated Green-Kubo transport coefficients in classical molecular dynamics as a readout problem for a quantum algorithm by representing Liouville evolution as unitary time evolution in the Koopman-von Neumann (KvN) framework. Both NVE dynamics and Nosé-Hoover-type NVT dynamics were described by Hermitian KvN generators within a common phase-space Hilbert-space framework, with the latter acting on the

TABLE I. **Resource scaling of the one-step propagators and the  $\hat{H}_3$  block.** The NVE circuit is a split-operator circuit consisting of QFTs and diagonal phase gates and can be implemented with  $\mathcal{O}(n^2)$  CX gates per step. In the present NVT circuit,  $U_3 = e^{-i\delta t \hat{H}_3}$  appears twice, and the  $\mathcal{O}(n_\xi n_p 2^{n_p})$  term from the centered-difference Pauli-decomposition method is dominant.

Level	Block or method	CX scaling
One-step propagator	NVE	$\mathcal{O}(n^2)$
One-step propagator	NVT with Pauli $\hat{H}_3$	$\mathcal{O}(n^2 + n_\xi n_p 2^{n_p})$
$\hat{H}_3$ block	QSD	$\mathcal{O}(4^{n_{\text{total}}})$
$\hat{H}_3$ block	Centered-difference Pauli decomposition	$\mathcal{O}(n_\xi n_p 2^{n_p})$
$\hat{H}_3$ block	QSP best case	$\mathcal{O}(n_{\text{total}} 2^{n_p})$

extended phase space including the thermostat variable. In finite-grid numerical benchmarks, we identified time regimes in which the KvN correlation functions agree with classical MD references, and we observed algebraic decay of the correlation-function discretization error with the number of grid points  $N_z$ . Thus, when the grid is represented by a quantum register with  $N_z = 2^{n_z}$ , this finite-grid error decreases exponentially with the number of qubits  $n_z$  assigned to that axis.

QPE provides the readout primitive for the transport coefficient in this formulation. When the flux-excited state is supplied as the system-register input, the ancilla bin-zero probability  $P_0$  determines the Bartlett-windowed Green–Kubo estimator. For the diffusion coefficient, this relation gives

$$D_{\text{Bart}} = \frac{1}{2} C_{vv}(0) \tau_{\text{QPE}} P_0. \quad (126)$$

In this way, evaluating the Green–Kubo integral is reformulated as the task of estimating the QPE-defined probability  $P_0$ , rather than as a sequential integration of the time-correlation function.

Given a canonical-state-preparation oracle and the QPE oracle defining  $P_0$ , we numerically verified the quadratic query-complexity improvement provided by MLAE for the statistical estimation of  $P_0$ . Direct shot sampling reduces the estimation error as  $N_{\text{queries}}^{-1/2}$ , whereas MLAE gives scaling close to  $N_{\text{queries}}^{-1}$  in the numerical regime studied here. Consequently, for the statistical error of the corresponding Bartlett-windowed Green–Kubo estimator, the required number of queries is improved from  $\mathcal{O}(\epsilon^{-2})$  to  $\mathcal{O}(\epsilon^{-1})$ .

For NVT dynamics, we showed that classical dynamics with a Nosé–Hoover thermostat can also be represented as unitary KvN evolution. In the present centered-difference Pauli-decomposition implementation, the friction term  $\hat{H}_3$  has a gate cost scaling as  $\mathcal{O}(n_\xi n_p 2^{n_p})$ . Within the explicit circuit syntheses examined in this work, this term is the dominant cost of the NVT one-step propagator. Reading correlation functions directly under NVT dynamics with polynomial gate cost would

therefore require a polynomial-cost block encoding of  $\hat{H}_3$ , or an alternative discretization or implementation of the thermostat term.

Two main directions remain for future work. The first is the efficient construction of the canonical-state-preparation oracle. This cost must be assessed separately from the query complexity of the Green–Kubo readout analyzed here. The second is to connect the KvN-MD framework to electronic-structure calculations performed on a quantum computer, by providing a concrete interface through which forces, potential-energy surfaces, or free-energy information are passed to the nuclear KvN dynamics. Such an interface would allow the quantum computation of electronic-structure information and the Green–Kubo readout formulated in this work to be combined within a single transport-coefficient calculation.

## ACKNOWLEDGMENTS

The author thanks Naoki Mitsumoto and Hidehiko Hiramatsu of DENSO CORPORATION, as well as the members of Quemix Inc., for valuable contributions and discussions. This work was supported by the Center of Innovation for Sustainable Quantum AI, JST Grant Number JPMJPF2221. The computation was performed using the facilities of the Supercomputer Center, the Institute for Solid State Physics, the University of Tokyo (ISSPkyodo-SC-2026-Ea-0014), the TSUBAME4.0 supercomputer at the Institute of Science Tokyo, and the Supermicro ARS-111GL-DNHR-LCC and FUJITSU Server PRIMERGY CX2550 M7 (Miyabi) at Joint Center for Advanced High Performance Computing (JC-AHPC).

## Appendix A: Stability of Discretized KvN Dynamics

In this appendix, we examine the stability of the finite-grid KvN evolution used in the main text. On a quantum computer, phase space is represented by a finite set of grid points, and each phase-space axis is encoded in a finite qubit register. It is therefore useful to separate the errors arising from boundary truncation, grid resolution, and time discretization. We use a one-particle model to identify which numerical parameters control these errors.

We mainly consider three types of errors. The first is the wrap-around error caused by truncating nonperiodic axes, such as the momentum  $p$  and the thermostat variable  $\xi$ , to finite intervals. The second is the grid-resolution error associated with representing the wave function on a finite number of grid points. The third is the time-discretization error introduced when the continuous-time evolution  $\exp(-i\hat{H}_{\text{KvN}}t)$  is approximated by the second-order symmetric Suzuki–Trotter product formula. Our purpose is not to combine these contributions into a single error estimate, but rather to

distinguish their physical origins and the parameters that suppress them.

### 1. Test Model and Error Metric

For the test system, we use the one-dimensional cosine potential

$$V(q) = V_0 \cos q, \quad q \in [0, 2\pi). \quad (\text{A1})$$

The coordinate  $q$  is a physically periodic variable. By contrast, the momentum  $p$  and the Nosé–Hoover variable  $\xi$  are nonperiodic variables and are numerically truncated to the finite intervals

$$p \in [-p_{\max}, p_{\max}), \quad \xi \in [-\xi_{\max}, \xi_{\max}). \quad (\text{A2})$$

We use  $V_0 = m = T_0 = Q = 1$  as the reference parameter set. The thermal widths are

$$\sigma_p = \sqrt{mT_0}, \quad \sigma_\xi = \sqrt{T_0/Q}, \quad (\text{A3})$$

and the boundary widths are specified as  $p_{\max} = n_\sigma \sigma_p$  and  $\xi_{\max} = n_\sigma \sigma_\xi$ .

The initial state is the equilibrium state, evaluated on the grid, that would be returned by the canonical-state-preparation oracle assumed in Sec. III B. Thus, for NVE, we use  $\psi_{\text{can}}(q, p) \propto \exp[-\beta H_{\text{cl}}(q, p)/2]$ , whereas for NVT, we use the corresponding extended state obtained by multiplying this state by  $\exp[-\beta Q\xi^2/4]$ . The NVT calculations in this appendix are intended to test the stability of time evolution generated by the Nosé–Hoover KvN generator on a discrete grid. They do not assume an efficient procedure for preparing the canonical state from an arbitrary initial state.

As a stability metric, we use the kinetic temperature

$$T_{\text{kin}}(t) = \frac{1}{N_f} \sum_{i=1}^{N_f} \left\langle \frac{\hat{p}_i^2}{m_i} \right\rangle_t. \quad (\text{A4})$$

Since  $T_{\text{kin}} = T_0$  in canonical equilibrium, we use the relative drift at a fixed observation time  $T_{\text{sim}}$ ,

$$\delta_T = \frac{|T_{\text{kin}}(T_{\text{sim}}) - T_0|}{T_0}, \quad (\text{A5})$$

as a representative measure of the discretization error. In Fig. 9, we set  $T_{\text{sim}} = 240$  and compare three time steps,  $\Delta t = 0.01, 0.05, 0.1$ .

### 2. Boundaries of Nonperiodic Axes and Wrap-Around Error

The  $q$  axis is physically periodic and is therefore compatible with Fourier differentiation. By contrast, the  $p$  and  $\xi$  axes are intrinsically nonperiodic. When Fourier

differentiation is used on a finite grid, however, these finite intervals are numerically treated as periodically connected. Consequently, if the tail of the probability density reaches a boundary, an unphysical wrap-around from  $+z_{\max}$  to  $-z_{\max}$  occurs, where  $z$  denotes either  $p$  or  $\xi$ .

This effect is particularly transparent for the Nosé–Hoover variable. The region  $\xi > 0$  is a cooling region in which momenta are damped, whereas  $\xi < 0$  is a heating region in which momenta are amplified. If the tail of the  $\xi$  distribution wraps from  $+\xi_{\max}$  to  $-\xi_{\max}$ , components on the cooling side are unphysically transferred to the heating side, producing a temperature drift. Similarly, wrap-around along the  $p$  axis distorts high-momentum components and their correlation with the force field, thereby degrading long-time temperature stability.

The nonperiodic components of the canonical distribution have Gaussian tails, so the relative density at the boundary is suppressed as

$$\frac{\varrho(z_{\max})}{\varrho(0)} = \exp\left(-\frac{n_\sigma^2}{2}\right). \quad (\text{A6})$$

Thus, as a first approximation, the temperature drift caused by the boundary decreases as

$$\delta_T^{\text{wrap}} \simeq A_z \exp\left(-\frac{n_\sigma^2}{2}\right). \quad (\text{A7})$$

Here  $A_z$  is a coefficient that depends on the force field, the observation time, and the time step. This exponential dependence is not a strict universal law, but it is useful as a diagnostic when the dominant error source is the probability mass reaching the boundary.

Figures 9(a) and 9(b) directly test this estimate by scanning the boundary width. For both the  $\xi$  and  $p$  axes, the temperature drift decreases approximately along  $\exp(-n_\sigma^2/2)$  in the range  $n_\sigma = 3$ –5, and for  $n_\sigma \gtrsim 6$ , the boundary error becomes smaller than the other error sources. In the calculations below, we therefore use

$$p_{\max} \gtrsim 6\sigma_p, \quad \xi_{\max} \gtrsim 6\sigma_\xi \quad (\text{A8})$$

as reference boundary conditions for the nonperiodic axes. These values are also consistent with empirical velocity-space truncation rules used in Fourier-type continuum Vlasov calculations [29–32].

### 3. Grid Resolution and the Time-Discretization Floor

After the boundary width is made sufficiently large, the remaining errors are controlled by the number of grid points and the time step. Figures 9(c) and 9(d) show the results obtained by fixing either  $\xi_{\max}$  or  $p_{\max}$  to  $8\sigma$  and varying  $N_\xi$  and  $N_p$ . In the low-resolution regime, even when the Gaussian tail is contained within the truncated interval, the wave function and its derivatives are not sufficiently resolved, and the temperature drift remains large. In contrast, the drift decreases rapidly for

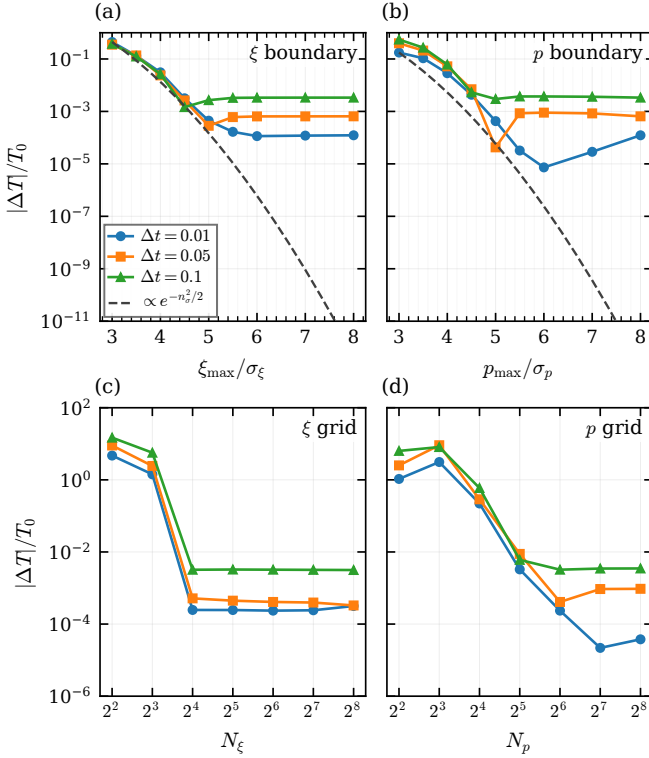


FIG. 9. **Stability of discretized KvN dynamics.** The test system is a one-particle NVT cosine potential with  $V_0 = m = T_0 = Q = 1$ ,  $T_{\text{sim}} = 240$ , and  $\Delta t \in \{0.01, 0.05, 0.1\}$ . (a) Boundary-width scan for the  $\xi$  axis. (b) Boundary-width scan for the  $p$  axis. The dashed line is the Gaussian-tail diagnostic proportional to  $\exp(-n_\sigma^2/2)$ . (c) Grid-size scan for the  $\xi$  axis. (d) Grid-size scan for the  $p$  axis. For sufficiently large boundary widths and grid sizes, the temperature drift reaches a floor determined by  $\Delta t$ .

$N_\xi, N_p \gtrsim 16$ , and for  $N_\xi, N_p \gtrsim 32$ , it nearly reaches the floor associated with each value of  $\Delta t$ .

This floor is consistent with the time-discretization error of the second-order symmetric Suzuki–Trotter product formula. The  $S_2(\Delta t)$  used in Sec. II D has a local error of  $\mathcal{O}(\Delta t^3)$  per step, and therefore the global error over a fixed physical time  $T$  is expected to scale as

$$\delta_T^{\text{ST}} \sim C_{\text{ST}} T \Delta t^2 + \mathcal{O}(\Delta t^4). \quad (\text{A9})$$

[21–25]. In each panel of Fig. 9, the floor reached after the boundary is made sufficiently wide or the grid sufficiently fine increases in the order  $\Delta t = 0.01, 0.05, 0.1$ , supporting this interpretation.

In summary, the temperature drift near equilibrium can be practically decomposed as

$$\delta_T \simeq C_{\text{ST}} T \Delta t^2 + A_p \exp\left(-\frac{p_{\text{max}}^2}{2\sigma_p^2}\right) + A_\xi \exp\left(-\frac{\xi_{\text{max}}^2}{2\sigma_\xi^2}\right) + \delta_T^{\text{grid}}. \quad (\text{A10})$$

TABLE II. **Guidelines for the discretization conditions in the one-particle one-dimensional cosine potential.** The boundary widths of the nonperiodic axes are expressed in terms of the thermal widths  $\sigma_p = \sqrt{mT_0}$  and  $\sigma_\xi = \sqrt{T_0/Q}$ .

Quantity	Guideline	Control
$p_{\text{max}}$	$\gtrsim 6\sigma_p$	$p$ wrap-around
$\xi_{\text{max}}$	$\gtrsim 6\sigma_\xi$	$\xi$ wrap-around
$N_p$	$\gtrsim 32$	$p$ resolution
$N_\xi$	$\gtrsim 32$	$\xi$ resolution
$N_q$	Resolve modes of $V(q)$	$q$ resolution
$\Delta t$	Converge $S_2(\Delta t)$	time-discretization floor

Here  $\delta_T^{\text{grid}}$  is the residual contribution from finite grid resolution. In the settings of Figs. 9(c) and 9(d), it becomes smaller than the time-discretization floor for  $N_p, N_\xi \gtrsim 32$ . Although this expression is not a rigorous error bound, it serves as a practical design formula for tuning the boundary width, grid resolution, and time step independently.

#### 4. Recommended Discretization and the $N = 2^n$ Grid Representation

Table II summarizes the practical discretization conditions inferred from Fig. 9 for the one-particle one-dimensional cosine potential. These values are representative for the present model. Systems with stiffer potentials, lower-temperature distributions, or longer correlation times require separate convergence checks for the boundary width, number of grid points, and time step.

The important point for quantum computation is that the number of grid points along each axis grows with the number of qubits as

$$N_z = 2^{n_z}. \quad (\text{A11})$$

Thus, increasing the grid resolution from  $N_z$  to  $2N_z$  requires adding only one qubit to the corresponding register. In a classical state-vector representation, memory grows in proportion to the product of the numbers of grid points as the phase-space dimension increases. In a quantum state representation, by contrast, the grid is encoded in qubit registers. This distinction becomes important when large  $N_z$  is needed to suppress discretization errors.

This statement does not mean that discretization errors disappear automatically. Sufficient boundary widths, sufficient grid resolution, and a sufficiently small  $\Delta t$  are still required. Moreover, even if the grid can be encoded using  $n_z$  qubits, a quantum-computational advantage can be realized only if the time-evolution operator is implemented with polynomial gate cost. As shown in the resource analysis, the NVE one-step propagator admits an  $\mathcal{O}(n^2)$  split-operator implementation, whereas in NVT, the term  $\hat{H}_3 = -\hat{\xi} \otimes \hat{D}_p$  becomes an  $\mathcal{O}(n_\xi n_p 2^{n_p})$

bottleneck in the present implementation. Thus, the conclusion of this appendix is twofold: it gives grid conditions under which the discretization error can be controlled, and it separates the representation-level benefit of quantum registers from the remaining implementation bottleneck in the NVT propagator.

In the actual diffusion-coefficient readout in this paper, we assume as input the equilibrium state supplied by the canonical-state-preparation oracle, and we mainly use the NVE propagator for the subsequent correlation-function evaluation. Therefore, the NVT stability analysis is intended to validate the Nosé–Hoover KvN generator itself; it does not imply that the controlled unitary in QPE must always be the NVT propagator. In Sec. IV, we test, under these discretization conditions, how accurately the velocity autocorrelation function is reproduced as a KvN inner product.

### Appendix B: Derivation of the QPE Bin-Zero Probability and the Bartlett Window

In the main text, we used the fact that the bin-zero probability obtained by applying QPE to the flux-excited state  $|\alpha_{\mathcal{D}}\rangle$  gives a finite-window Bartlett-windowed Green–Kubo estimator. This appendix gives the algebraic derivation of Eqs. (87)–(??) in the main text.

We first define the finite Dirichlet kernel

$$D_K(\theta) = \sum_{r=0}^{K-1} e^{-ir\theta}. \quad (\text{B1})$$

Using the finite geometric series, this can be written as

$$D_K(\theta) = e^{-i(K-1)\theta/2} \frac{\sin(K\theta/2)}{\sin(\theta/2)}. \quad (\text{B2})$$

Therefore,

$$|D_K(\theta)|^2 = \frac{\sin^2(K\theta/2)}{\sin^2(\theta/2)}. \quad (\text{B3})$$

For  $\theta = 2\pi n$ , with integer  $n$ , this expression is understood by continuity as  $|D_K|^2 = K^2$ .

The same quantity can also be expressed as a double sum:

$$|D_K(\theta)|^2 = \sum_{r=0}^{K-1} \sum_{r'=0}^{K-1} e^{-i(r-r')\theta}. \quad (\text{B4})$$

For a fixed difference  $s = r - r'$ , the number of pairs  $(r, r')$  with that difference is  $K - |s|$ , for  $|s| \leq K - 1$ .

Hence,

$$|D_K(\theta)|^2 = \sum_{s=-(K-1)}^{K-1} (K - |s|) e^{-is\theta} \quad (\text{B5})$$

$$= K + \sum_{s=1}^{K-1} (K - s) (e^{-is\theta} + e^{+is\theta}) \quad (\text{B6})$$

$$= K + 2 \sum_{s=1}^{K-1} (K - s) \cos(s\theta). \quad (\text{B7})$$

Equations (B3) and (B7) are the squared-Dirichlet-kernel identities used in the main text.

Next, let  $U_{\mathcal{D}} |\phi_k\rangle = e^{-i\theta_k} |\phi_k\rangle$ , and expand the flux-excited state as

$$|\alpha_{\mathcal{D}}\rangle = \sum_k a_k |\phi_k\rangle. \quad (\text{B8})$$

For an  $m_{\text{anc}}$ -qubit QPE circuit with  $K = 2^{m_{\text{anc}}}$ , the bin-zero probability is

$$P_0 = \sum_k |a_k|^2 \frac{|D_K(\theta_k)|^2}{K^2}. \quad (\text{B9})$$

Substituting Eq. (B7) gives

$$P_0 = \frac{1}{K^2} \left[ K + 2 \sum_{s=1}^{K-1} (K - s) \sum_k |a_k|^2 \cos(s\theta_k) \right]. \quad (\text{B10})$$

On the other hand,

$$\text{Re} \langle \alpha_{\mathcal{D}} | U_{\mathcal{D}}^s | \alpha_{\mathcal{D}} \rangle = \text{Re} \sum_k |a_k|^2 e^{-is\theta_k} \quad (\text{B11})$$

$$= \sum_k |a_k|^2 \cos(s\theta_k) = c_{\mathcal{D}}(s\Delta t). \quad (\text{B12})$$

Thus, the bin-zero probability can be written as

$$P_0 = \frac{1}{K^2} \left[ K + 2 \sum_{s=1}^{K-1} (K - s) c_{\mathcal{D}}(s\Delta t) \right]. \quad (\text{B13})$$

Finally, multiplying Eq. (B13) by  $\frac{1}{2} C_{JJ}^{(\mathcal{D})}(0) \tau_{\text{QPE}}$  and using  $\tau_{\text{QPE}} = K\Delta t$ , we obtain

$$\begin{aligned} \frac{1}{2} C_{JJ}^{(\mathcal{D})}(0) \tau_{\text{QPE}} P_0 &= C_{JJ}^{(\mathcal{D})}(0) \Delta t \\ &\times \left[ \frac{1}{2} + \sum_{s=1}^{K-1} \left( 1 - \frac{s}{K} \right) c_{\mathcal{D}}(s\Delta t) \right]. \end{aligned} \quad (\text{B14})$$

This is the discrete Green–Kubo estimator obtained by applying the Bartlett window

$$w_s = 1 - \frac{s}{K}, \quad s = 0, 1, \dots, K,$$

together with the trapezoidal-rule coefficient 1/2 at  $s = 0$ . The window vanishes at  $s = K$ , so no endpoint contribution appears there. For a diffusion coefficient, setting  $C_{JJ} = C_{vv}$  gives Eq. (92) in the main text.

### Appendix C: Details of the Centered-Difference Pauli-Decomposition Method

This appendix summarizes the centered-difference Pauli-decomposition method used in Sec. VII A. The target operator is the momentum-dilation generator appearing in the Nosé–Hoover friction term,

$$\hat{H}_3 = -\hat{\xi} \otimes \hat{D}_p, \quad \hat{D}_p = \frac{1}{2} (\hat{p}\hat{\lambda}_p + \hat{\lambda}_p\hat{p}). \quad (\text{C1})$$

Here  $n_p$  denotes the number of qubits in the momentum register, and  $N_p = 2^{n_p}$  is the number of momentum grid points.

In the benchmark code used for the resource analysis, the momentum grid is defined as

$$p_j = p_{\min} + j\Delta p, \\ \Delta p = \frac{p_{\max} - p_{\min}}{N_p}, \quad j = 0, \dots, N_p - 1, \quad (\text{C2})$$

and a cyclic centered difference is used as the finite-difference operator. That is, the indices are treated modulo  $N_p$ , so a wrap-around bond between  $j = N_p - 1$  and  $j = 0$  is included. This is the same convention as that used in the circuit-resource measurements in Fig. 6.

With this convention, the Hermitian discrete dilation operator is

$$\hat{D}_p^{\text{cyc}} = -i \sum_{j=0}^{N_p-1} \gamma_j (|j+1\rangle \langle j| - |j\rangle \langle j+1|), \\ \gamma_j = \frac{p_j + p_{j+1}}{4\Delta p}, \quad (\text{C3})$$

where  $j+1$  is understood modulo  $N_p$ . Equation (C3) is the centered-difference discretization of the continuous operator  $(\hat{p}\hat{\lambda}_p + \hat{\lambda}_p\hat{p})/2$ . If a nonperiodic momentum window is used, the endpoint treatment can be modified separately. The gate counts in Figs. 6 and 8, however, are based on the cyclic convention in Eq. (C3).

We expand Eq. (C3) in the Pauli basis on the  $n_p$ -qubit computational basis:

$$\hat{D}_p^{\text{cyc}} = \sum_{\mu \in \mathcal{S}_{D_p}} a_\mu P_\mu, \quad P_\mu \in \{I, X, Y, Z\}^{\otimes n_p}, \quad a_\mu \in \mathbb{R}. \quad (\text{C4})$$

Equation (C3) is a purely imaginary antisymmetric matrix. Therefore, only Pauli strings containing an odd number of  $Y$  operators can have nonzero coefficients. Indeed, if  $N_Y(P_\mu)$  denotes the number of  $Y$  operators in  $P_\mu$ , then

$$P_\mu^* = (-1)^{N_Y(P_\mu)} P_\mu.$$

Pauli strings with an even number of  $Y$  operators are real matrices and have zero Hilbert–Schmidt inner product with Eq. (C3). We refer to this selection rule as the odd- $Y$  filter.

The number of terms in the Pauli expansion can be counted by classifying the nearest-neighbor bonds  $|j+1\rangle \langle j|$  according to the carry length in the binary representation of  $j$ . A longer carry in the update  $j \rightarrow j+1$  produces Pauli strings with larger weight. The cyclic bond  $N_p - 1 \rightarrow 0$  introduces the longest carry and therefore increases the number of Pauli terms compared with a nonperiodic finite-difference operator. Combining this carry structure with the odd- $Y$  filter gives the number of nonzero Pauli strings as

$$N_{D_p}^{\text{cyc}}(n_p) \equiv |\mathcal{S}_{D_p}| = \frac{7}{4} 2^{n_p} - (n_p + 2), \quad n_p \geq 2. \quad (\text{C5})$$

This closed form corresponds to the Pauli decomposition used in the Pauli-evolution benchmark in Fig. 6.

The circuit-cost estimate depends not only on the number of Pauli terms but also on the Pauli-string weights. We define the weight  $w(P_\mu)$  as the number of nonidentity Pauli operators in  $P_\mu$ , and define the weighted Pauli sum by

$$W_{D_p}^{\text{cyc}}(n_p) \equiv \sum_{\mu \in \mathcal{S}_{D_p}} w(P_\mu). \quad (\text{C6})$$

A single Pauli rotation  $\exp(-i\theta P_\mu)$  can be implemented using basis changes, a CNOT ladder, one  $R_z$  rotation, and the inverse ladder. Thus,  $w(P_\mu)$  determines the leading contribution to the two-qubit gate count for that rotation.

For the Pauli expansion of Eq. (C3), the weighted Pauli sum is

$$W_{D_p}^{\text{cyc}}(n_p) = \frac{7}{4} n_p 2^{n_p} - 3 \cdot 2^{n_p} + 3, \quad n_p \geq 2. \quad (\text{C7})$$

Therefore, the centered-difference Pauli-decomposition method gives

$$N_{D_p}^{\text{cyc}}(n_p) = \mathcal{O}(2^{n_p}), \quad W_{D_p}^{\text{cyc}}(n_p) = \mathcal{O}(n_p 2^{n_p}). \quad (\text{C8})$$

Equivalently, since  $N_p = 2^{n_p}$ , the weighted Pauli sum scales as

$$\mathcal{O}(N_p \log N_p)$$

with the number of momentum grid points, and hence exponentially with the number of momentum qubits  $n_p$ .

Finally, we include the tensor product with  $\hat{\xi}$ . The coordinate operator  $\hat{\xi}$  is diagonal on the  $\xi$  register, and under binary encoding it can be expanded as

$$\hat{\xi} = \sum_{\nu \in \mathcal{S}_\xi} b_\nu Z_\nu, \quad Z_\nu \in \{I, Z\}^{\otimes n_\xi}. \quad (\text{C9})$$

For a coordinate operator on an equally spaced grid, the number of nonzero  $Z$ -string terms is  $\mathcal{O}(n_\xi)$ . Hence

$$\hat{H}_3 = - \sum_{\nu \in \mathcal{S}_\xi} \sum_{\mu \in \mathcal{S}_{D_p}} b_\nu a_\mu Z_\nu \otimes P_\mu, \quad (\text{C10})$$

and the leading cost of a Pauli-evolution implementation is

$$\mathcal{O}(n_\xi W_{D_p}^{\text{cyc}}(n_p)) = \mathcal{O}(n_\xi n_p 2^{n_p}). \quad (\text{C11})$$

The growth of the NVT cost shown in Figs. 6 and 8 originates from this exponential dependence on the momentum-register size  $n_p$  in the present centered-difference Pauli-decomposition implementation.

#### Appendix D: Evaluation Method and Oracle Assumptions for the QSP Best-Case Line

This appendix summarizes how the QSP best-case line in Fig. 6 is evaluated. The green series in that figure is not obtained by transpiling an implemented quantum circuit in Qiskit. Rather, it is a theoretical CX estimate for Hamiltonian simulation by QSP under a sparse-access oracle model for the sparse-matrix representation of  $\hat{H}_3$ .

The target operator is

$$\hat{H}_3 = -\hat{\xi} \otimes \hat{D}_p. \quad (\text{D1})$$

The  $\hat{D}_p$  used in the benchmark code is the nearest-neighbor finite-difference matrix based on the cyclic centered difference, with nonzero bond coefficients

$$\gamma_j = \frac{p_j + p_{j+1}}{4\Delta p}, \quad j+1 \equiv j+1 \pmod{N_p}. \quad (\text{D2})$$

The row sparsity with respect to the  $p$  register is therefore  $d = 2$ .

For the best-case line, we assume the following two sparse-access oracles:

$$O_{\text{loc}} : |i\rangle | \ell \rangle \mapsto |i\rangle |j_\ell(i)\rangle, \quad \ell = 0, 1, \quad (\text{D3})$$

$$O_{\text{val}} : |i\rangle |j\rangle |0\rangle \mapsto |i\rangle |j\rangle \left| \langle \hat{H}_3 \rangle_{ij} \right\rangle. \quad (\text{D4})$$

Here  $O_{\text{loc}}$  returns the nonzero column indices in row  $i$ , and  $O_{\text{val}}$  returns the corresponding matrix element to fixed-point precision. This oracle model differs from a Pauli-LCU circuit that directly implements a sum of Pauli strings through SELECT operations. Thus, the best-case line in Fig. 6 should be regarded as a theoretical target that would be reachable only if these sparse-access oracles were available at low cost.

In the sparse-access model, we use an upper bound based on the row-sum norm as the block-encoding normalization factor. In the benchmark of this work, this factor is taken as

$$\alpha_{\text{sparse}} = 2 \|\hat{H}_3\|_{\text{max}} = 2 \xi_{\text{max}} \max_j |\gamma_j|. \quad (\text{D5})$$

Here  $\xi_{\text{max}} = (2^{n_\xi} - 1)\Delta\xi/2$ . If the  $p$  and  $\xi$  windows are fixed, then  $\Delta p = \mathcal{O}(2^{-n_p})$ , and Eq. (D5) gives  $\alpha_{\text{sparse}} = \mathcal{O}(2^{n_p})$ .

In QSP, the normalized operator  $M = \hat{H}_3/\alpha_{\text{sparse}}$  is used to approximate

$$e^{-i\delta t \hat{H}_3} = e^{-i\tau M}, \quad \tau = \delta t \alpha_{\text{sparse}}. \quad (\text{D6})$$

In the benchmark, we set  $\delta t = \text{dt\_half} = 0.01$ , and choose the truncation degree  $K_{\text{QSP}}$  of the Jacobi–Anger expansion from the condition

$$|J_{K_{\text{QSP}}+1}(\tau)| < \epsilon_{\text{qsp}}/2. \quad (\text{D7})$$

Here  $J_m$  is the Bessel function. Asymptotically, this condition gives

$$K_{\text{QSP}} = \mathcal{O}\left(\tau + \log \frac{1}{\epsilon_{\text{qsp}}}\right) = \mathcal{O}\left(2^{n_p} + \log \frac{1}{\epsilon_{\text{qsp}}}\right). \quad (\text{D8})$$

In the present setting, we use  $\epsilon_{\text{qsp}} = 10^{-6}$ .

Following the convention of the benchmark code, the CX count for a single sparse block-encoding primitive is estimated as

$$C_{\text{BE}}^{\text{sparse}} = 6n_{\text{total}} + 3n_{\text{total}} + \left\lceil n_{\text{total}} \log_2 \left( \frac{1}{\epsilon_{\text{qsp}}} \right) \right\rceil + n_{\text{total}}. \quad (\text{D9})$$

The four terms represent, respectively, the row oracle, the value oracle, an RUS-arcsin-type amplitude transformation, and overheads such as reflections. The integer rounding corresponds to the `int` operation in the benchmark code. For  $\epsilon_{\text{qsp}} = 10^{-6}$ , we have  $\log_2(1/\epsilon_{\text{qsp}}) \simeq 19.9$ , so  $C_{\text{BE}}^{\text{sparse}}$  is approximately  $30n_{\text{total}}$ .

For the full QSP estimate, we use the convention

$$N_{\text{BE}}^{\text{best}} = 4K_{\text{QSP}} + 3, \quad N_{\text{ref}}^{\text{best}} = 2K_{\text{QSP}} + 2. \quad (\text{D10})$$

Counting each reflection layer as  $4n_{\text{total}}$  CX gates, the green line in Fig. 6 is given by

$$N_{\text{CX}}^{\text{QSP,best}} = (4K_{\text{QSP}} + 3)C_{\text{BE}}^{\text{sparse}} + (2K_{\text{QSP}} + 2)4n_{\text{total}}. \quad (\text{D11})$$

Equations (D8) and (D9) imply the leading scaling

$$N_{\text{CX}}^{\text{QSP,best}} = \mathcal{O}(n_{\text{total}} 2^{n_p}). \quad (\text{D12})$$

As a numerical reproduction example, take  $n_p = 10$ ,  $n_\xi = 4$ ,  $\epsilon_{\text{qsp}} = 10^{-6}$ , and  $\delta t = 0.01$ . Then  $n_{\text{total}} = 14$ ,  $\alpha_{\text{sparse}} = 1918.125$ ,  $\tau = 19.18125$ , and  $K_{\text{QSP}} = 34$ . The block-encoding cost is

$$C_{\text{BE}}^{\text{sparse}} = 6(14) + 3(14) + \lceil 14 \log_2(10^6) \rceil + 14 = 419, \quad (\text{D13})$$

and Eq. (D11) gives

$$N_{\text{CX}}^{\text{QSP,best}} = (4 \cdot 34 + 3)419 + (2 \cdot 34 + 2)4 \cdot 14 = 62161. \quad (\text{D14})$$

This is the same convention as that used for the best-case series in Fig. 6.

This estimate is a theoretical reference for the case in which the sparse structure of  $\hat{H}_3$  can be accessed through low-cost oracles. Therefore, in Fig. 6, it should not be interpreted as the same type of data as the transpiled CX counts for the native Pauli circuit or the QSD circuit. Instead, it is used as a best-case reference for a possible implementation based on a more efficient block encoding of the Nosé–Hoover friction term.

## Appendix E: Validation by Quantum-Circuit Simulation

This appendix verifies that the circuits constructed in Sec. III reproduce the same propagators and QPE ancilla-bin distributions as the discrete KvN state-vector calculation. The main text presents the circuit construction; here we collect the numerical checks of the circuit-level implementation.

### 1. Validation Design

The quantum-circuit simulations are performed in two stages. First, to validate  $S_2^D(\Delta t)$  without QPE ancillas, we compare the discrete KvN state-vector calculation with the Qiskit state-vector simulation. As the observable, we use the reduced phase-space distribution of particle 1,

$$P^{(1)}(q_1, p_1; t) = \sum_{q_2, p_2} |\langle q_1, p_1, q_2, p_2 | \psi(t) \rangle|^2. \quad (\text{E1})$$

This provides a direct comparison of the probability distribution on the system register, independently of any QPE ancilla measurement.

Second, we validate the full QPE circuit. We compare the ancilla-bin probability distribution  $\{P_\ell^{\text{KvN}}\}$  computed from the discrete KvN state vector with  $\{P_\ell^{\text{circ}}\}$  obtained from the Qiskit state-vector simulation. In addition, in shot-based simulations, we estimate the bin-zero frequency  $\hat{P}_0$  from a finite number of shots and examine the mean and standard deviation of

$$\hat{D} = \frac{1}{2} C_{vv}(0) \tau_{\text{QPE}} \hat{P}_0. \quad (\text{E2})$$

The fluctuations observed in this test are the statistical errors of Bernoulli trials with success probability  $P_0$ . These are the errors targeted by the amplitude-estimation procedure discussed in Sec. VI.

### 2. Agreement of Reduced Phase-Space Distributions

Figure 10 compares the reduced phase-space distributions for the two-particle coupled cosine system. For the system register composed of the  $q$  and  $p$  registers of each particle, we repeatedly apply the same one-step propagator and evaluate  $P^{(1)}(q_1, p_1; t)$  at  $t = 2.56$ . The distributions obtained from the discrete KvN state-vector calculation and from the Qiskit state-vector simulation agree after propagation, with a maximum difference of  $\sim 2 \times 10^{-15}$ . This difference is within double-precision roundoff error, confirming that the split-operator circuit reproduces the discrete KvN propagator.

This check is independent of the QPE ancilla distribution. The QPE bin probabilities are projections onto

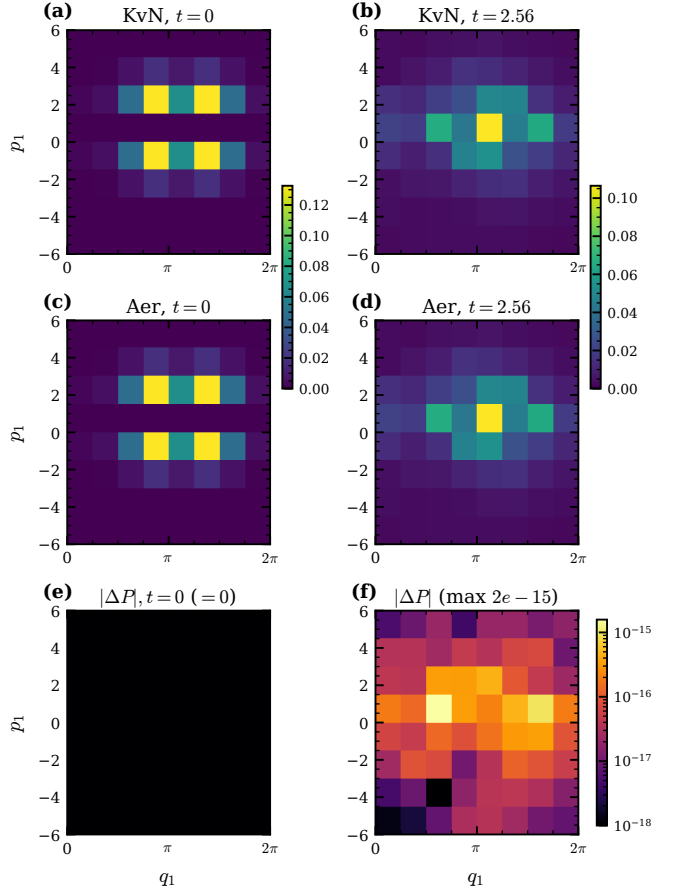


FIG. 10. **Validation of the one-step propagator using reduced phase-space distributions.** For the two-particle coupled cosine system, we compare the reduced phase-space distribution  $P^{(1)}(q_1, p_1; t)$  of particle 1. The top row shows the discrete KvN state-vector calculation, the middle row shows the Qiskit state-vector simulation, and the bottom row shows the bin-wise differences. The difference is numerically zero at the initial time, and after propagation to  $t = 2.56$ , the maximum difference remains approximately  $2 \times 10^{-15}$ , as indicated in the figure.

the eigenphase distribution, whereas Fig. 10 compares the probability distribution on the system register itself. Agreement at this level confirms that the KvN propagator circuit has no structural error before it is used as the controlled unitary in phase estimation.

### 3. QPE Ancilla-Bin Distribution and Finite-Shot Statistics

Figure 11(a) shows the convergence of  $\hat{D}$  when the same QPE circuit is executed with a finite number of shots. Here we use  $m_{\text{anc}} = 7$ , corresponding to  $K = 2^7$ . Since  $\Delta t = 0.02$ ,

$$\tau_{\text{QPE}} = K \Delta t = 2^{m_{\text{anc}}} \Delta t = 2.56. \quad (\text{E3})$$

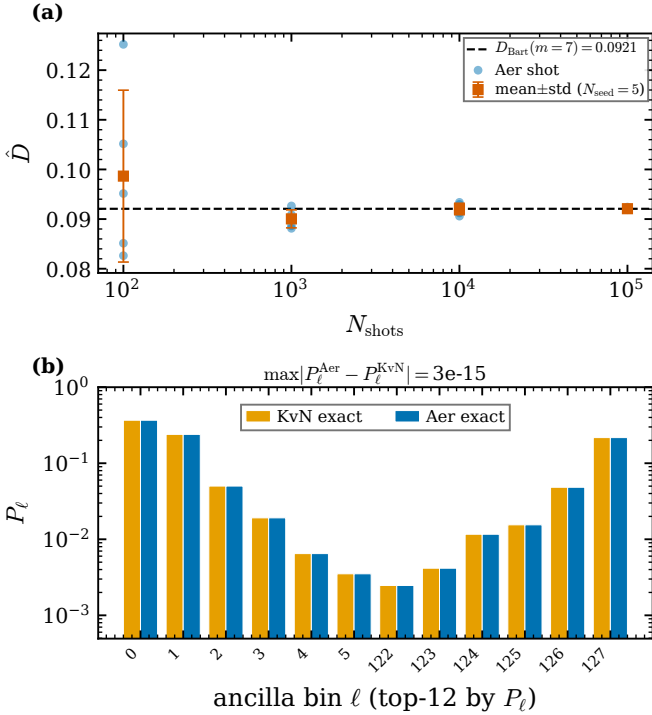


FIG. 11. **Ancilla-bin distribution and finite-shot statistics from QPE circuit simulations.** (a) Convergence of  $\hat{D}$  estimated with a finite number of shots. The black dashed line is the state-vector value  $D_{\text{Bart}}(m_{\text{anc}} = 7) = 0.0921$ ; individual points are shot-based simulations with independent seeds, and squares denote the mean and standard deviation. (b) Comparison of the QPE ancilla-bin probability distributions. The plotted bins are the 12 bins with the largest probabilities, and the maximum difference over all bins is  $\max_{\ell} |P_{\ell}^{\text{circ}} - P_{\ell}^{\text{KvN}}| \simeq 3 \times 10^{-15}$ , as indicated in the figure.

The target value obtained from the state-vector simulation is  $D_{\text{Bart}}(m_{\text{anc}} = 7) = 0.0921$ , and the mean of  $\hat{D}$  converges to this value as the number of shots is increased. The standard deviation decreases according to

$$\sigma(\hat{D}) \simeq \frac{1}{2} C_{vv}(0) \tau_{\text{QPE}} \sqrt{\frac{P_0(1-P_0)}{N_{\text{shots}}}}. \quad (\text{E4})$$

This scaling follows because the bin-zero measurement is a Bernoulli trial.

Figure 11(b) shows the state-vector simulation of the QPE circuit. The ancilla-bin distribution obtained from the discrete KvN calculation and that obtained from the Qiskit state-vector simulation agree over all bins to within machine precision. This confirms that the full QPE circuit, including the controlled-  $U^{2^j}$  gates, the inverse QFT, and the bit ordering convention, generates the same ancilla probability distribution as the discrete KvN state-vector calculation.

Together, these two simulations show that the circuits constructed in Sec. III reproduce both the discrete KvN propagator and the QPE bin-zero readout at the state-vector level. The remaining finite-shot error is not a circuit-construction error, but the statistical error in estimating  $P_0$ . This statistical error is the target of the amplitude-estimation method discussed in Sec. VI.

- 
- [1] M. E. Tuckerman, *Statistical Mechanics: Theory and Molecular Simulation* (Oxford University Press, 2023).
- [2] R. Fallahzadeh and N. Farhadian, *Solid State Ionics* **280**, 10 (2015).
- [3] A. Baktash, J. C. Reid, T. Roman, and D. J. Searles, *npj Computational Materials* **6**, 162 (2020).
- [4] A. Muralidharan, M. I. Chaudhari, L. R. Pratt, and S. B. Rempe, *Scientific Reports* **8**, 10736 (2018).
- [5] I. Kassal, S. P. Jordan, P. J. Love, M. Mohseni, and A. Aspuru-Guzik, *Proc. Natl. Acad. Sci. U.S.A.* **105**, 18681 (2008).
- [6] J. D. Whitfield, J. Biamonte, and A. Aspuru-Guzik, *Mol. Phys.* **109**, 735 (2011).
- [7] Y. Su, D. W. Berry, N. Wiebe, N. Rubin, and R. Babush, *PRX Quantum* **2**, 040332 (2021).
- [8] P. J. Ollitrault, A. Miessen, and I. Tavernelli, *Acc. Chem. Res.* **54**, 4229 (2021).
- [9] I. Joseph, *Phys. Rev. Research* **2**, 043102 (2020).
- [10] S. Simon, R. Santagati, M. Degroote, N. Moll, M. Streif, and N. Wiebe, *PRX Quantum* **5**, 010343 (2024).
- [11] P.-W. Huang, G. Boyd, G.-L. R. Anselmetti, M. Degroote, N. Moll, R. Santagati, M. Streif, B. Ries, D. Marti-Dafcik, H. Jnane, S. Simon, N. Wiebe, T. R. Bromley, and B. Koczor, arXiv **arXiv:2508.16719**, 10.48550/arXiv.2508.16719 (2025), arXiv:2508.16719.
- [12] S. Nosé, *J. Chem. Phys.* **81**, 511 (1984).
- [13] W. G. Hoover, *Phys. Rev. A* **31**, 1695 (1985).
- [14] B. O. Koopman, *Proc. Natl. Acad. Sci. U.S.A.* **17**, 315 (1931).
- [15] J. v. Neumann, *Annals of Mathematics* **33**, 587 (1932).
- [16] G. Brassard, P. Høyer, M. Mosca, and A. Tapp, in *Quantum Computation and Information*, Contemporary Mathematics, Vol. 305 (American Mathematical Society, 2002) pp. 53–74.
- [17] Y. Suzuki, S. Uno, R. Raymond, T. Tanaka, T. Onodera, and N. Yamamoto, *Quantum Inf. Process.* **19**, 75 (2020).
- [18] D. Grinko, J. Gacon, C. Zoufal, and S. Woerner, *npj Quantum Inf.* **7**, 52 (2021).
- [19] D. I. Bondar, F. Gay-Balmaz, and C. Tronci, *Proc. R. Soc. A* **475**, 20180879 (2019).
- [20] G. J. Martyna, M. L. Klein, and M. Tuckerman, *J. Chem. Phys.* **97**, 2635 (1992).
- [21] H. F. Trotter, *Proceedings of the American Mathematical Society* **10**, 545 (1959).

- [22] M. Suzuki, *Communications in Mathematical Physics* **51**, 183 (1976).
- [23] M. Suzuki, *Phys. Lett. A* **146**, 319 (1990).
- [24] H. Yoshida, *Phys. Lett. A* **150**, 262 (1990).
- [25] I. D. Kivlichan, C. Gidney, D. W. Berry, N. Wiebe, J. McClean, W. Sun, Z. Jiang, N. Rubin, A. Fowler, A. Aspuru-Guzik, H. Neven, and R. Babbush, *Quantum* **4**, 296 (2020).
- [26] J. Welch, D. Greenbaum, S. Mostame, and A. Aspuru-Guzik, *New J. Phys.* **16**, 033040 (2014).
- [27] B. Leimkuhler and C. Matthews, *J. Chem. Phys.* **138**, 174102 (2013).
- [28] A. Javadi-Abhari, M. Treinish, K. Krsulich, C. J. Wood, J. Lishman, J. Gacon, S. Martiel, P. D. Nation, L. S. Bishop, A. W. Cross, B. R. Johnson, and J. M. Gambetta, *Quantum computing with Qiskit* (2024), [arXiv:2405.08810](https://arxiv.org/abs/2405.08810) [quant-ph].
- [29] C. Z. Cheng and G. Knorr, *J. Comput. Phys.* **22**, 330 (1976).
- [30] A. J. Klimas, *J. Comput. Phys.* **68**, 202 (1987).
- [31] A. J. Klimas and W. M. Farrell, *J. Comput. Phys.* **110**, 150 (1994).
- [32] G. V. Vogman, P. Colella, and U. Shumlak, *J. Comput. Phys.* **277**, 101 (2014).
- [33] V. V. Shende, S. S. Bullock, and I. L. Markov, *IEEE Trans. Comput.-Aided Des. Integr. Circuits Syst.* **25**, 1000 (2006).
- [34] A. M. Childs and N. Wiebe, *Quantum Inf. Comput.* **12**, 901 (2012).
- [35] G. H. Low and I. L. Chuang, *Quantum* **3**, 163 (2019).